# Chemomechanical Simulation of Microtubule Dynamics With Explicit Lateral Bond Dynamics

Matthias Schmidt and Jan Kierfeld*

Department of Physics, TU Dortmund University, Dortmund, Germany

We introduce and parameterize a chemomechanical model of microtubule dynamics on the dimer level, which is based on the allosteric tubulin model and includes attachment, detachment and hydrolysis of tubulin dimers as well as stretching of lateral bonds, bending at longitudinal junctions, and the possibility of lateral bond rupture and formation. The model is computationally efficient such that we reach sufficiently long simulation times to observe repeated catastrophe and rescue events at realistic tubulin concentrations and hydrolysis rates, which allows us to deduce catastrophe and rescue rates. The chemomechanical model also allows us to gain insight into microscopic features of the GTP-tubulin cap structure and microscopic structural features triggering microtubule catastrophes and rescues. Dilution simulations show qualitative agreement with experiments. We also explore the consequences of a possible feedback of mechanical forces onto the hydrolysis process and the GTP-tubulin cap structure.

Keywords: microtubule dynamics, dynamic instability, chemomechanical model, catastrophes, hydrolysis, microtubule, cytoskeleton

## 1. INTRODUCTION

Microtubule (MT) dynamics is essential for many cellular processes, such as the positioning and separation of chromosomes in mitosis [1], or maintenance of cell polarity and cell shape [2]. An important feature, which enables MTs to exert pulling and pushing forces in these cellular processes, is their dynamic instability, which is the stochastic switching of MTs between states of growth by polymerization and states of fast shrinkage by depolymerization [3].

Switching from growth into shrinkage happens in catastrophe events, whose mechanism and triggers are not completely understood on the molecular level, but they are associated with a loss of the GTP-cap by hydrolysis within the MT [4, 5] (see references [6, 7] for reviews). Hydrolysis is strongly coupled to mechanics of the MT, as is clearly seen in the curling of MT protofilaments into a "ram's horn" conformation after the catastrophe and during the shrinking phase [8]. The loss of the stabilizing GTP-cap triggers a release of binding energy and stored mechanical energy in the tubular MT structure. Therefore, shrinkage following a catastrophe is more than simple depolymerization of the MT; it is rather a rupture or crack propagation process between protofilaments, which releases chemical and mechanical energy while it propagates toward the minus end. The energy released during shrinking has biological functions and can be employed to exert pulling forces onto kinetochores during separation of MTs in mitosis [9].

The curling of hydrolyzed protofilaments into a ram's horn structure shows that GDP-tubulin dimers have a bent conformation [8, 10–12]. Tubulin dimers assembled within the MT body are in a straight conformation, on the other hand [13]. Hydrolysis of tubulin dimers embedded in a straight MT causes mechanical strains in the tubular structure because the surrounding MT lattice prevents these GDP-tubulin dimers from assuming their preferred bent conformation. This mechanical strain is released in a catastrophe via the rupture of lateral bonds.

There are different models explaining how the mechanical strain is increased by hydrolysis or how lateral bonds are weakened by hydrolysis such that the strained MT becomes more prone for catastrophes. The first cryo-electron microscopy (EM) studies showed blunt tips for growing MTs but curved tips for shrinking MTs [8] suggesting that GTP-protofilaments are straight while GDP-protofilaments are curved. Later evidence from cryo-EM showed that GTP-protofilaments are also curved, but significantly less than GDP-protofilaments [10]. The *allosteric model* is based on the assumption that hydrolysis of a tubulin dimer changes the dimer conformation from a rather straight GTP-conformation to a bent GDP-conformation. Hydrolysis of tubulin dimers embedded in a straight MT causes mechanical strain in the tubular structure because the surrounding MT lattice prevents these GDP-tubulin dimers from assuming their preferred bent conformation. This model was employed in almost all previous MT simulation models that consider MT mechanics [14–19]. The *lattice model*, on the other hand, is based on evidence from X-ray and cryo-EM structures [20–23] and simulations [24, 25] that also GTP-tubulin dimers assume a bent conformation and that hydrolysis rather affects the lateral and longitudinal dimer interaction energies. It is supported by recent experimental observations that both growing and shrinking MTs have bent protofilament ends [26]. Reference [26] also presents first simulation results with a lattice model. But there is also recent evidence from molecular dynamics (MD) simulation pointing in a different direction and supporting an intermediate model, where hydrolysis affects interactions but also lowers GDP-tubulin flexibility [27]. If hydrolysis weakens lateral interaction energies, hydrolysis makes the MT structure more prone for a catastrophe. While in the allosteric model, the mechanical strain in the structure is increased by hydrolysis, in the lattice model, the mechanical strain that the MT structure can tolerate is reduced by hydrolysis. In both models, the result is an increased propensity for lateral bonds to rupture. Therefore, chemomechanical MT models with explicit bond rupture are a necessity to reproduce catastrophes. We build on existing modeling approaches based on the allosteric model [14–19] and include lateral bond rupture as explicit stochastic events with force-dependent rates, which can give important clues about how catastrophes are triggered in the MT structure.

The influence of tubulin dimer hydrolysis onto the mechanics of the MT lattice suggests that, vice versa, mechanical forces and torques acting on tubulin dimers via strains in the tubular structure could also affect hydrolysis rates, an effect which has been explored only in reference [17] previously. Although this interplay is plausible from a mechanochemistry point of view, experimental verification on the dimer level is extremely difficult and not possible yet, but we can employ chemomechanical MT models to explore and suggest possible implications for the dynamic instability.

The coupling between chemical events—namely polymerization events, dimer hydrolysis, bond rupture—and mechanical forces because of conformational changes due to these chemical events, is a characteristic of MTs and requires chemomechanical MT models on the dimer level in order to develop a microscopic understanding of their dynamic instability including catastrophe and rescue events [28]. In this respect, chemomechanical models go beyond a phenomenological description of MT dynamics in a four-parameter model based on growth and shrinking velocities and phenomenological catastrophe and rescue rates [29]. The challenge for microscopic chemomechanical models is to include all chemical events as stochastic processes, to perform conformational relaxation governed by MT mechanics following each chemical event, and, eventually, to also include the feedback of mechanical forces within the MT onto reaction rates of the chemical events.

We present a stochastic chemomechanical MT model on the dimer level. Our model includes (i) a mechanical model of the MT containing lateral elastic bonds between tubulin monomers in neighboring protofilaments and a harmonic bending energy between tubulin monomers with a non-zero equilibrium angle after hydrolysis (allosteric model), (ii) stochastic addition and removal of tubulin dimers, (iii) explicit stochastic lateral bond rupture and bond formation; the bond rupture rate is coupled to the mechanical stress state of the bond and thus via elastic interactions within the MT lattice also to the other bonds, (iv) stochastic hydrolysis of dimers with a rate that can also couple to the mechanical bending stress in the dimer. The stochastic kinetics (ii)–(iv) is handled by a Gillespie algorithm and after each stochastic event, a mechanical energy minimization mimicking the relaxational dynamics of the structure is applied to the MT.

In order to parameterize our model, we will focus on the simplified scenarios of a growing MT consisting of GTP-tubulin only and a shrinking MT consisting of GDP-tubulin only. In both cases, we can neglect hydrolysis (iv); in the growing GTP-MT, we can also neglect mechanics, which is generated by hydrolysis. In the presence of mechanics and hydrolysis, repeated catastrophe and rescue events are obtained and will be described and analyzed. One problem in chemomechanical MT models is the computational effort associated with the mechanical relaxation. We investigate in detail, which level of computational effort is necessary in our model to obtain a sufficient mechanical relaxation following each chemical event, on the one hand, and which simplifications can be taken to assure a finite simulation time for growing MTs, on the other hand. This will allow us to simulate arbitrarily long growing MTs at fixed computational speed.

Our chemomechanical model has to be compared to previous modeling approaches, which include the mechanics of the MT [14–19]:

- References [15, 16] employ the allosteric model for dimer bending and include stochastic addition and removal of dimers. Hydrolysis is random. Mechanical energy

minimization is performed only locally on randomly selected dimers. Lateral bond rupture is not implemented as explicit stochastic process but only included using a threshold energy criterion.

- The models in references [14, 19] focus on mechanics and do not include dimer addition and removal. They are also based on the allosteric model but consider fixed hydrolysis states. In reference [14], the lateral bond energy landscape is harmonic around a minimum but includes an energy barrier and a dissociated, i.e., ruptured state. Global energy minimization gives the final state of the static structure.
- In reference [18], the stochastic kinetics is added to a mechanical model similar to Molodtsov et al. [14]. Here, the mechanical relaxation and lateral bond rupture is performed using Brownian dynamics (which include thermal fluctuations) with small time steps (equivalent to $2 \times 10^7$ minimization steps), which is only applied to 300 tubulin dimers at the plus end. Stochastic addition of dimers and removal by rupture of lateral and longitudinal bonds is included. The rupture of lateral bonds happens by activation over the bond energy barrier, the longitudinal rupture by a threshold criterion. Hydrolysis is random and stochastic with a rate that is independent of mechanics.
- Reference [17] is also based on the allosteric model. Lateral bond rupture is possible using a threshold criterion. Mechanical energy minimization was performed globally. There is no addition or removal of dimers, but hydrolysis is included. In a first attempt to include a coupling of the hydrolysis rate to mechanical forces, the hydrolysis kinetics remained deterministic, however, with the most probable hydrolysis event determined by mechanical forces. In the present paper, we will add addition and removal of dimers and a fully stochastic hydrolysis kinetics.

Our chemomechanical model has also to be compared to previous purely chemical modeling approaches on the dimer level but without explicit mechanical model [30–34]. These models include attachment and detachment of tubulin dimers; some of these models [32–34] also include lateral bond rupture and are thus able to produce crack-like catastrophe events. Crack-like catastrophe events are, however, triggered by adjusting chemical rupture rates rather than including MT mechanics. The model by Margolin et al. [33] has successfully reproduced features of the experimentally observed MT dynamic instability [35] but relies on a heuristic tuning of simulation parameters.

## 2. MATERIALS AND METHODS

### 2.1. Microtubule Structure and Energy

Our MT model is formulated on the dimer level. The base units of the model are alpha- and beta-tubulin monomers. In our model, we represent each monomer as cylinder with radius $r_t = 2\,nm$ and height $\ell_t = 4\,nm$ (see **Table 1**). Alpha- and beta-tubulin monomers form unbreakable tubulin dimers, which are arranged head-to-tail into protofilaments. Thirteen protofilaments form a 13_3 MT, i.e., a MT with a helical shift of three tubulin monomer lengths per turn.

**TABLE 1 |** Geometric parameters of our MT model.

| Parameter | Symbol | Value |
| --- | --- | --- |
| Mean MT radius | $R_{MT}$ | 10.5 nm |
| Tubulin monomer radius | $r_t$ | 2 nm |
| Tubulin monomer length | $\ell_t$ | 4 nm |
| Helical shift between protofilaments | $\Delta z_h$ | 0.92 nm |
| Rest length of lateral springs | $s_0$ | 1.47 nm |
| Straight equilibrium bending angle | $\Delta\theta_0$ | 0° |
| Curved equilibrium bending angle | $\Delta\theta_0$ | 11° |

For the remainder of this paper, we will use triples $(p, d, t)$ to address specific tubulin monomers within the MT with $p \in \{1, 2, \ldots, 13\}$ as the protofilament number, $d \in \{1, 2, \ldots, d(p)\}$ as the tubulin layer [with $d = 1$ denoting the minus end and $d = d(p)$ denoting the plus end of the protofilament $p$], and $t \in \{1, 2\}$ denoting the tubulin monomer within the dimer with $t = 1$ for the alpha- and $t = 2$ for the beta-tubulin monomers. For simplicity, we assume periodicity in $p$ (i.e., $p = 0 \equiv 13$ and $p = 14 \equiv 1$) and combined periodicity in $d$ and $t$ [i.e., $(p, d, 3) \equiv (p, d + 1, 1)$ and $(p, d, 0) \equiv (p, d - 1, 2)$]. We will also generally refer to the lateral neighbors of tubulin monomer $(p, d, t)$ using $(p \pm 1, d, t)$ even though at the seam, lateral neighbors differ in all three indices.

The MT is straight and oriented along the $z$-axis with the positive $z$-direction pointing to the plus end. Vectors $\vec{m}(p, d, t)$ and $\vec{p}(p, d, t)$ point to the to the lower (minus end) and upper (plus end) circular base of the tubulin monomer $(p, d, t)$. The direction vector

$$\vec{d}(p, d, t) = \vec{p}(p, d, t) - \vec{m}(p, d, t) = \ell_t \begin{pmatrix} \cos\phi(p)\sin\theta(p, d, t) \\ -\sin\phi(p)\sin\theta(p, d, t) \\ \cos\theta(p, d, t) \end{pmatrix}$$

(1)

with length $\ell_t = 4\,nm$ points from $\vec{m}(p, d, t)$ to $\vec{p}(p, d, t)$ and is specified using spherical coordinates, i.e., azimuthal and polar angles (see **Figure 1A**). The polar angle $\theta(p, d, t)$ is the only degree of freedom of each monomer, because we assume that monomers can only be displaced in radial direction, i.e., all azimuthal angles are fixed to $\phi(p) = 2\pi(p-1)/13$. As both alpha- and beta-tubulin have their polar angles as a degree of freedom, the model supports intra- and inter-dimer curling [36].

At the minus end of the MT each protofilament $p$ starts with an alpha-tubulin arranged in a circle with mean MT radius $R_{MT} = 10.5\,nm$ and with an offset $z(p, 1, 1) = 3\ell_t(p - 1)/13$ in $z$-direction, such that the seam is between the 13th and the 1st protofilament. The protofilament length that will be used to calculate the growth and shrinkage velocities is the maximum $z$-coordinate $\ell_{max}(p)$ of all tubulin monomers within the protofilament (see **Supplementary Material** for more details). The MT length is given by the average

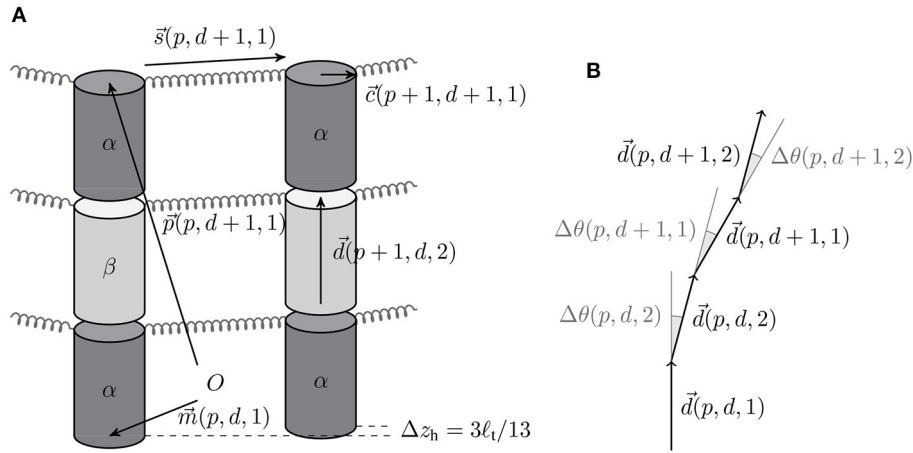$$\ell_{MT} = \frac{1}{13} \sum_{p=1}^{13} \ell_{max}(p).$$

(2)

**FIGURE 1 | (A)** Schematic illustration of the different vectors with the origin $O$ (The vertical gaps between tubulin cylinders are for illustration purposes only). **(B)** Bending angles between the tubulin monomer direction vectors.

Every tubulin monomer has four interaction points: two in longitudinal direction and two in lateral direction. The longitudinal bond between alpha- and beta-tubulin monomers of the same dimer is considered unbreakable but the orientation of this junction can change via the beta-tubulin's polar angle $\theta(p, d, 2)$. In contrast, the longitudinal bond between adjacent tubulin monomers of different dimers can break and is modeled via the bond energy $\Delta G_{\text{long}}^{0*}$ (where the "0" refers to it being a standard energy [37] and the asterisk to the fact that it also includes the entropic cost of "immobilization" [30]). The lateral interaction points are located at the edge of the upper base (see **Figure 1A**). If there is a lateral bond between tubulin monomer $(p, d, t)$ and its neighbor in the $(p + 1)$-th protofilament, the bond is modeled as a harmonic spring with base energy $\Delta G_{\text{lat}}^0$:

$$E_{\text{lat}}(p, d, t) = \Delta G_{\text{lat}}^0 + \frac{1}{2} k_{\text{lat}} \left( |\vec{s}(p, d, t)| - s_0 \right)^2 \quad (3)$$

with the spring constant $k_{\text{lat}}$ of the bond and the vector $\vec{s}(p, d, t)$ connecting the lateral interaction points; $s_0 \simeq 1.47 \, nm$ is the rest length of the spring (see [17] and also consider the helical shift between two neighboring tubulin monomers of $3\ell_t/13$). Lateral bonds at the seam are assumed to have identical mechanical properties as other lateral bonds based on evidence that they do not constitute a weaker bond [22, 38]. Additionally, there is a lateral repulsion term between neighboring tubulin monomers (regardless of whether they are bonded or not) to ensure a cylindrical form [17]:

$$E_{\text{rep}}(p, d, t) = k_{\text{rep}} \left( |\vec{p}(p, d, t) - \vec{p}(p + 1, d, t)| - 2r_t \right)^{-12}. \quad (4)$$

The bending of monomer junctions is described by a harmonic potential with bending constant $\kappa$:

$$E_{\text{bend}}(p, d, t) = \frac{1}{2} \kappa \left( \Delta\theta(p, d, t) - \Delta\theta_0(p, d, t) \right)^2. \quad (5)$$

The bending angle $\Delta\theta(p, d, t) = \theta(p, d, t) - \theta(p, d, t - 1)$ (see **Figure 1B**) is calculated with the neighboring monomer in the minus direction [using the periodicity convention in $d$ and $t$, $(p, d, 0) \equiv (p, d - 1, 2)$], and $\Delta\theta_0(p, d, t)$ is its equilibrium value. For hydrolyzed beta-tubulin monomers and for alpha-tubulin monomers on top of a hydrolyzed beta-tubulin (and for the first alpha-tubulin monomers of each protofilament if the beta-tubulin in the same dimer is hydrolyzed), we use a rest angle $\Delta\theta_0(p, d, t) = 11°$ in order to reproduce the experimentally measured radius of curvature of 21 nm corresponding to an angle of $22°$ per dimer for a GDP-protofilament curling into the ram's horn configuration [10, 39]. Otherwise (for an unhydrolyzed beta-tubulin monomer or an alpha-tubulin monomer on top of an unhydrolyzed beta-tubulin monomer), we assume a straight equilibrium configuration with $\Delta\theta_0(p, d, t) = 0°$. This choice of rest angles implements the allosteric model, where GTP-hydrolysis leads to bending of tubulin dimers.

Our mechanical MT model is defined by the total energy

$$E_{\text{MT}} = \sum_{p=1}^{13} \sum_{d=1}^{d(p)} \left( \Delta G_{\text{long}}^{0*} + \sum_{t=1}^{2} \left[ E_{\text{lat}}(p, d, t) + E_{\text{rep}}(p, d, t) \right. \right.$$
$$\left. \left. + E_{\text{bend}}(p, d, t) \right] \right), \quad (6)$$

where $E_{\text{lat}}(p, d, t)$ only contributes if there is a lateral bond between tubulin monomers $(p, d, t)$ and $(p + 1, d, t)$ and $E_{\text{rep}}(p, d, t)$ only contributes if tubulin monomer $(p, d, t)$ has a lateral partner $(p + 1, d, t)$.

There are four free parameters in our mechanical MT model (see **Table 2**): the longitudinal bond energy $\Delta G_{\text{long}}^{0*}$, the lateral bond energy $\Delta G_{\text{lat}}^0$, the lateral spring constant $k_{\text{lat}}$, and the bending constant $\kappa$. For the repulsion constant $k_{\text{rep}}$, we use the same value $k_{\text{rep}} = 10^{-6} \, rad^2 \, nm^{12} \kappa$ that has been found previously to ensure the overall cylindrical shape of the MT and only contributes a small portion to the MT energy [17].

**TABLE 2 |** Free parameters of our MT model and the "standard set" of their values that we will focus on in the rest of the paper.

| Parameter | Symbol | Standard set of values |
|---|---|---|
| Longitudinal bond energy | $\Delta G_{\text{long}}^{0*}$ | $-9.3\,k_{\text{B}}T$ |
| Lateral bond energy | $\Delta G_{\text{lat}}^{0}$ | $-1.58\,k_{\text{B}}T$ |
| Lateral spring constant | $k_{\text{lat}}$ | $100\,k_{\text{B}}T/\text{nm}^2$ |
| Bending constant | $\kappa$ | $149\,k_{\text{B}}T/\text{rad}^2$ |
| Pseudo-first-order polymerization rate | $k_+$ | $4\,\mu\text{M}^{-1}\,\text{s}^{-1}$ |
| Lateral bond formation attempt rate | $k_{\text{att}}$ | $258\,\text{s}^{-1}$ |
| Constant hydrolysis rate | $k_{\text{hydr}}$ | $0.1$–$0.5\,\text{s}^{-1}$ |
| Base hydrolysis rate | $k_{\text{hydr}}^{0}$ | $1$–$5\,\text{s}^{-1}$ |



**FIGURE 2 | (A)** Schematic illustration of the different simulation events with their rates. Dashed lateral bonds can be formed with rate $k_{\text{form}}$, thin solid lateral bonds can rupture with rate $k_{\text{rup}}$, and thick bond cannot rupture. "T" and "D" correspond to the hydrolysis state of beta-tubulin of the dimers. **(B)** If the black tubulin dimer in layer $d$ is affected by an event and $d_{\text{cutoff}} = 2$ was used, all of the gray (and the black) tubulin dimers are used for energy minimization.

In the simulation model, we do not use this mechanical energy to calculate forces for a microscopic dynamics, such as Brownian dynamics on the dimer level (as opposed to [18]). We rather assume that mechanical relaxation dynamics is fast compared to chemical changes in the MT due to tubulin attachment and detachment, bond rupture and formation, or hydrolysis. The slowest mechanical process is relaxation of bending modes of protofilaments governed by small restoring bending moments. The basic time scale for this process can be estimated as $\tau \sim \eta \ell_t^3/\kappa$ [40], where $\eta \sim 10^{-3}\,Pa\,s$ is the viscosity of water. This gives $\tau \sim 10^{-10}\,s$, which is orders of magnitude smaller than typical time scales of seconds for chemical events. Therefore, even longer protofilaments relax fast compared to chemical changes. There is additional evidence from Brownian dynamics that bending mode relaxation is also much faster than immobilization in cryo-EM [41]. Therefore, we perform a quasi-instantaneous energy minimization of (6) between these chemical simulation steps. This is the computationally more efficient strategy to achieve mechanical relaxation. The rates of all chemical simulation events themselves determine the dynamics of the MT and are handled by a Gillespie algorithm as explained in more detail below.

## 2.2. Chemical Simulation Events

To simulate the dynamics of MTs, we include attachment of individual GTP-tubulin dimers and detachment of (laterally unbonded) tubulin dimers or whole (laterally unbonded) protofilament segments at the plus end, as well as lateral bond rupture and formation, and hydrolysis of tubulin dimers as stochastic chemical events into the simulation; **Figure 2A** summarizes the different possible events and the associated rates.

### 2.2.1. Attachment and Detachment

At the plus end of each protofilament, a GTP-tubulin dimer can attach with an on-rate

$$k_{\text{on}} = k_+ c_{\text{tub}} \tag{7}$$

where $k_+$ is the pseudo-first-order polymerization rate and $c_{\text{tub}}$ is the concentration of free GTP-tubulin dimers. The on-rate is assumed to be independent of the hydrolysis state of the protofilament end.
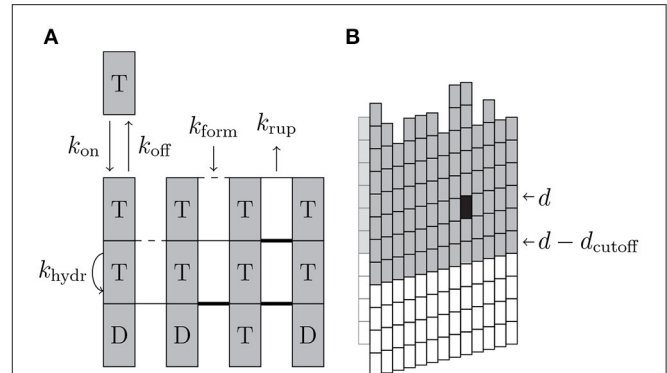
For depolymerization, we assume that a tubulin dimer at the plus end can only detach if it has no lateral bonds. We also allow for detachment of whole protofilament segments starting from an interior dimer $[d < d(p)]$ if the whole segment has no lateral bonds. Laterally unbounded dimers or segments can detach with a rate

$$k_{\text{off}} = k_+ c_0 \exp\left(\Delta G_{\text{long}}^{0*}\right) \tag{8}$$

as given by Kramers theory with the longitudinal standard bond energy $\Delta G_{\text{long}}^{0*}$ (including the entropic cost of "immobilization") and the standard concentration $c_0 = 1\,M$ [37].

This approach differs from other models [15, 30, 42], where tubulin dimers can detach regardless of whether they have lateral bonds or not. In such models, if a tubulin dimer still has lateral bonds, its detachment rate decreases exponentially with the additional lateral bond energies. In our model, we rather include lateral bond rupture and formation as separate stochastic events into the simulation (similarly to the purely chemical models in [32–34]); bond rupture can then be followed by detachment of laterally unbounded dimers or protofilament segments. Bond rupture enables dimer detachment and is necessary prior to a catastrophe; vice versa, bond reformation is necessary for a rescue event. Therefore, it is essential to also include the process of bond formation into the model. Moreover, it has been observed in MD simulations in Kononova et al. [43] that lateral tubulin bonds can easily reform. The restriction that only laterally unbonded dimers can detach also causes an indirect increase of the effective off-rate if the last dimers of a protofilament are hydrolyzed because this tends to create stretched bonds, which rupture more easily.

### 2.2.2. Zipper-Like Lateral Bond Rupture and Bond Formation

We assume that bond rupture between protofilaments starts from the plus end and proceeds by a rupture front monomer by monomer toward the minus end; likewise, bonds can be reformed

only monomer by monomer toward the plus end in a zipper-like fashion. As a result, we always have a rupture front between two neighboring protofilaments such that all monomers on top of the front toward the plus end are ruptured and all monomers below toward the minus end are intact. If tubulin monomer $(p, d, t - 1)$ has a lateral bond with its neighbor in protofilament $p + 1$ but the tubulin monomer on top of it, $(p, d, t)$, has no lateral bond with this neighbor, the rupture front can recede toward the plus end, and tubulin monomer $(p, d, t)$ can form a bond with rate

$$k_{\text{form}} = k_{\text{att}} \qquad (9)$$

with the attempt rate $k_{\text{att}}$. Vice versa, if the bond at $(p, d, t)$ is intact and bond $(p, d, t + 1)$ is broken, the rupture front can advance toward the minus end by rupturing this bond with a rate

$$k_{\text{rup}} = k_{\text{att}} \exp \left( \Delta G_{\text{lat}}^0 + \Delta G_{\text{mech}} \right) \qquad (10)$$

which contains the chemical lateral bond energy $\Delta G_{\text{lat}}^0$ and a mechanical energy $\Delta G_{\text{mech}}$, which accounts for the weakening of the lateral bond due to mechanical strain in the bond and enters according to Bell theory [44, 45]. In our model, $\Delta G_{\text{mech}}$ is due to the stretching of the Hookean springs representing the lateral bonds so that $\Delta G_{\text{mech}} = F_{\text{lat}} \ell_{\text{rup}}$, where $F_{\text{lat}} = -\partial E_{\text{lat}} / \partial |\vec{s}(p, d, t)|$ is the force currently acting on the lateral bond and $\ell_{\text{rup}}$ is the characteristic bond rupture length. We define $\ell_{\text{rup}}$ as the length increase of the lateral bond from its rest length $s_0$ at which the stretching energy of the spring cancels the bond energy:

$$\ell_{\text{rup}} = \sqrt{\frac{-2 \Delta G_{\text{lat}}^0}{k_{\text{lat}}}}. \qquad (11)$$

## 2.2.3. Hydrolysis Without and With Mechanical Feedback

Lastly, GTP in beta-tubulin monomers can hydrolyze into GDP via a random (or scalar) hydrolysis rule meaning that almost every GTP-tubulin dimer in the MT can hydrolyze with a fixed rate $k_{\text{hydr}}$ regardless of the hydrolysis state of its longitudinal neighbor (which would be a vectorial hydrolysis rule). The "almost" in the previous sentence refers to the finding that the polymerization of the tubulin dimer $(p, d)$ and thus the formation of a longitudinal bond between beta-tubulin $(p, d - 1, 2)$ and alpha-tubulin $(p, d, 1)$ catalyzes the hydrolysis reaction in beta-tubulin $(p, d - 1, 2)$ [13]. As a consequence, only GTP-tubulin dimers that ever had another tubulin dimer on top of them can be hydrolyzed in our model.

We also consider the possibility that hydrolysis is mechanochemically coupled to the bending strain [17]. Then, the hydrolysis rate

$$k_{\text{hydr}}(p, d) = k_{\text{hydr}}^0 \exp \left( -\Delta E_{\text{hydr}}(p, d) \right) \qquad (12)$$

is modulated with a dimer-specific change $\Delta E_{\text{hydr}}(p, d)$ in the energy barrier height of the hydrolysis reaction, which depends on the bending state of dimer $(p, d)$. Because this bending state also depends via lateral bonds on the bending states in

all neighboring dimers, and because the bending state of all neighboring dimers strongly depends on their hydrolysis state, the hydrolysis dynamics becomes effectively non-random but depends on the hydrolysis state of the neighbors.

The basis for our assumption of a tubulin dimer-specific mechanochemical hydrolysis rate is to view the equilibrium bending angle $\Delta \theta_0$ of a dimer as the reaction coordinate for hydrolysis which can be described by an energy profile $F_{\text{hydr}}(\Delta \theta_0)$. $F_{\text{hydr}}(\Delta \theta_0)$ has two local minima corresponding to the straight conformation with $\Delta \theta_0 = 0°$ and the curved conformation with $\Delta \theta_0 = 11°$ and a rate-limiting energy barrier of unknown height $\Delta F_{\text{hydr}}^{\text{barrier}}$ in between. We propose that hydrolysis of a tubulin dimer is eased if its actual bending angle $\Delta \theta$ is closer to the equilibrium angle $\Delta \theta_0 = 11°$ in the hydrolyzed state. We model this dependency by adding a dimer-specific bending energy contribution $E_{\text{hydr}}(\Delta \theta_0)$ to $F_{\text{hydr}}(\Delta \theta_0)$, which changes the energy barrier height from $\Delta F_{\text{hydr}}^{\text{barrier}}$ to $\Delta F_{\text{hydr}}^{\text{barrier}} + \Delta E_{\text{hydr}}(p, d)$ (see **Figure 3**). $\Delta F_{\text{hydr}}^{\text{barrier}}$ can be absorbed into the constant rate $k_{\text{hydr}}^0$ so that only $\Delta E_{\text{hydr}}(p, d)$ remains in the Arrhenius factor in (12).

To calculate the change in the energy barrier height $\Delta E_{\text{hydr}}(p, d)$, we now consider the total MT energy in (6) as a function of the hydrolysis reaction coordinate $\Delta \theta_0$ while keeping all polar angles $\{\theta(p, d, t)\}$ fixed. We simply assume that the energy barrier is centered between the minima at $\Delta \theta_0^{\text{barrier}} = 5.5°$ resulting in

$$\Delta E_{\text{hydr}} = E_{\text{MT}}(\Delta \theta_0 = 5.5°) - E_{\text{MT}}(\Delta \theta_0 = 0°). \qquad (13)$$

Because hydrolysis of tubulin dimer $(p, d)$ affects the rest bending angles of beta-tubulin monomer $(p, d, 2)$ and alpha-tubulin monomer $(p, d + 1, 1)$ and the rest bending angles only affect the
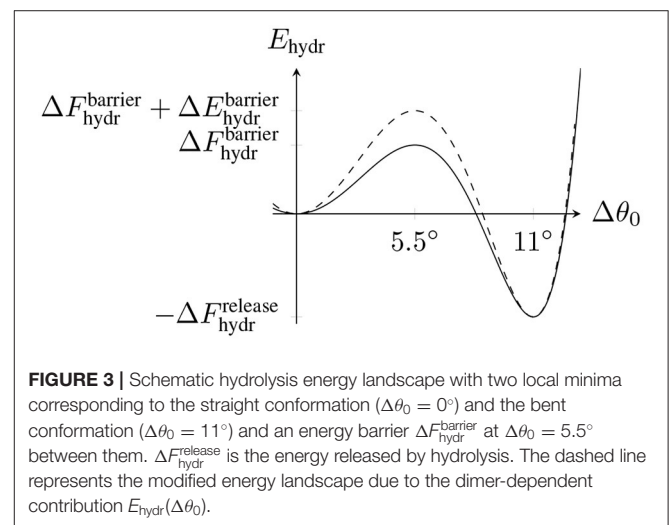
**FIGURE 3 |** Schematic hydrolysis energy landscape with two local minima corresponding to the straight conformation ($\Delta \theta_0 = 0°$) and the bent conformation ($\Delta \theta_0 = 11°$) and an energy barrier $\Delta F_{\text{hydr}}^{\text{barrier}}$ at $\Delta \theta_0 = 5.5°$ between them. $\Delta F_{\text{hydr}}^{\text{release}}$ is the energy released by hydrolysis. The dashed line represents the modified energy landscape due to the dimer-dependent contribution $E_{\text{hydr}}(\Delta \theta_0)$.

bending energies (5), we finally obtain

$$
\begin{aligned}
\Delta E_{\text{hydr}}(p, d) &= \frac{1}{2}\kappa\Big[(\Delta\theta(p, d, 2) - 5.5°)^2 - \Delta\theta^2(p, d, 2) \\
&\quad + (\Delta\theta(p, d + 1, 1) - 5.5°)^2 - \Delta\theta^2(p, d + 1, 1)\Big] \\
&= \frac{1}{2}\kappa\Big[-(\Delta\theta(p, d, 2) + \Delta\theta(p, d + 1, 1)) \cdot 11° \\
&\quad + 2 \cdot (5.5°)^2\Big]
\end{aligned}
\tag{14}
$$

so that only a local bending energy change has to be calculated. As a result, tubulin monomers in the MT lattice with larger bending angles $\Delta\theta(p, d, t)$ tend to hydrolyze preferentially. For the terminal tubulin dimer of a protofilament $(p, d(p))$, the $d + 1$-term in (14) is missing because tubulin monomer $(p, d(p) + 1, 1)$ does not exist. This results in an overall smaller energy barrier and, thus, a higher hydrolysis rate of the terminal tubulin dimer.

We also see that the base hydrolysis rate $k_{\text{hydr}}^0$ in (12) is not the hydrolysis rate for a perfectly straight MT $[\Delta\theta(p, d, t) = 0°$ for all tubulin monomers] because there is still the constant contribution $\kappa(5.5°)^2$ to the energy barrier in (14) that reduces the hydrolysis rate. As these terms are proportional to the bending constant $\kappa$, we cannot simply absorb them into the constant factor $k_{\text{hydr}}^0$.

We note that for almost all GTP-tubulin dimers in the GDP-body of the MT, we will typically find *negative* bending angles; these dimers bend inward in order to allow the longitudinal GDP-dimer neighbors to further bend outwards. For such negative bending angles the hydrolysis rate is reduced according to (14).

In addition to the previous four free parameters from the MT energy, the simulation events add three additional free parameters: the pseudo-first-order polymerization rate $k_+$, the attempt rate $k_{\text{att}}$, and the hydrolysis rate $k_{\text{hydr}}$ (or $k_{\text{hydr}}^0$). In total, there are now seven free parameters, which are listed in **Table 2**.

## 2.3. Simulation and Parameter Determination

The actual MT simulation (implemented in C++) works as follows:

1. Initially, a MT with $N_{\text{GDP}}$ GDP-tubulin dimers followed by $N_{\text{GTP}}$ GTP-tubulin dimers per protofilament is constructed with $\theta(p, d, t) = 0°$ for all $(p, d, t)$.
2. Using the tubulin monomers' polar angles $\{\theta(p, d, t)\}$, the MT's actual initial configuration is determined by minimizing its mechanical energy. Details on the minimization procedure will be discussed in the next section.
3. For all of the events described in the previous section, a list of possible events is determined and based on their rates $k_i$, a "tentative" event time $t_i$ is calculated using Gillespie's first reaction method [46]:

$$
t_i = \frac{1}{k_i}\ln\frac{1}{r}
\tag{15}
$$

where $r$ is a uniformly distributed random number from 0 to 1. The event $i$ with the shortest event time $t_i$ is executed and the simulation time is increased by $t_i$.

4. Assuming fast mechanical relaxation the MT's energy is minimized after any event.
5. The simulation terminates if a protofilament is shorter than two tubulin dimers.[1] Otherwise we go back to the third step to determine the next event.

There is a general agreement between different experiments [3, 47–52] that the MT growth velocity $v_{\text{gro}}$ increases linearly with the tubulin dimer concentration $c_{\text{tub}}$ and that the shrinkage velocity $v_{\text{shr}}$ is independent of $c_{\text{tub}}$. We will use the results by Walker et al. [47], which were measured for $c_{\text{tub}} \in [7.7, 15.5\,\mu M]$,

$$
v_{\text{gro}}(c_{\text{tub}}) = (0.33 \pm 0.01)\frac{\mu m}{min\,\mu M}c_{\text{tub}} - (1.59 \pm 0.50)\frac{\mu m}{min},
\tag{16}
$$

$$
v_{\text{shr}} = (-27 \pm 1)\frac{\mu m}{min},
\tag{17}
$$

and lead to an individual critical concentration $c_{\text{tub,c}} \simeq 5\,\mu M$ (below which $v_{\text{gro}} < 0$).

To determine the values of the model parameters, we use a "divide and conquer" approach [15, 30]. First, we consider MT growth, where mechanics are assumed not to play a significant role as protofilaments are not curling outward so that $\Delta G_{\text{mech}} = 0$. Thus, we use a GTP-only MT ($N_{\text{GDP}} = 0$) and set $k_{\text{lat}} = 0$ and $\kappa = 0$ so that the only free parameters left are $k_+$, $\Delta G_{\text{long}}^{0*}$, $\Delta G_{\text{lat}}^0$, and $k_{\text{att}}$. The goal of these simulations is to reproduce the measured growth velocity in (16) as function of the free tubulin dimer concentration $c_{\text{tub}}$. Secondly, we consider MT shrinkage, where mechanics are now assumed to play a significant role, i.e., $k_{\text{lat}} > 0$ and $\kappa > 0$. For a shrinking MT, we use $N_{\text{GTP}} = 0$, $N_{\text{GDP}} > 0$, and the parameter values already determined by the growth simulations to reproduce the shrinkage velocity in (17). In both cases, hydrolysis is ignored. A schematic overview of the entire parameter determination procedure can be found in **Figure S7** in the Supplementary Material.

Comparing the number of free parameters and the amount of experimental data, we can already predict that we will not be able to determine one set of fixed parameter values but only restrict some parameter values to specific values if other parameter values are set to (arbitrarily but reasonably) chosen values. We will discuss this issue in more detail in the conclusion.

## 2.4. Energy Minimization

In previous three-dimensional models, different energy minimization approaches have been used. VanBuren et al. [15] used a local minimization approach in which they randomly selected individual tubulin dimers and then only locally

---

[1]To calculate shrinkage velocities of shrinkage simulations via a simple linear fit, it has proven to be easier to stop simulations if a protofilament still contains one tubulin dimer instead of zero tubulin dimers as the last tubulin dimer requires more time to depolymerize creating a "tail" in the length-vs.-time plot. This time increase is due to lateral springs being stretched less because there is no additional tubulin dimer below the terminal tubulin dimer that would exert an additional bending moment. In practice, for determining parameters and when running full simulations, this first layer at the minus end is irrelevant and could be regarded as a "seed" on which the MT grows.

minimized with respect to the parameters of this dimer. On average, each tubulin dimer was visited three times for minimization. Zakharov et al. [18] employed a completely different approach by explicitly modeling the stochastic motion of tubulin monomers in space using Brownian dynamics (applied to the first 300 tubulin dimers at the plus end). They solve Langevin equations every $2 \times 10^{-10}$ s while using $10^{-3}$ s as the time step for the events in their simulation resulting in $\mathcal{O}(10^7)$ dynamics steps between actual events. Using a parallel implementation run on a supercomputer, their simulation took more than a day to simulate 1 s of MT dynamics. There are drawbacks for both approaches: a local energy minimization scheme might not come close enough to a mechanically relaxed configuration, whereas a full Brownian dynamics simulation is computationally very costly. In this paper, we employ a systematic mechanical energy minimization between each stochastic chemical simulation event. We try to achieve a better mechanical energy relaxation than VanBuren et al. [15] with significantly less computational steps than Zakharov et al. [18].

In our simulation, we use the Broyden–Fletcher–Goldfarb–Shanno (BFGS) algorithm, a quasi-Newton method, provided by the GNU Scientific Library (GSL) [53] to minimize the total mechanical MT energy in (6) as a function of the polar angles $\{\theta(p, d, t)\}$. If each protofilament in the simulated MT contains $N_{\mathrm{GDP}} + N_{\mathrm{GTP}}$ tubulin dimers, there are a total of $26(N_{\mathrm{GDP}} + N_{\mathrm{GTP}})$ polar angles and thus the same number of minimization parameters. In realistic simulations, MTs can stay in the growing phase for a very long time resulting in an unbounded increase in the number of minimization parameters drastically slowing down the simulation. In essence, the average time for one minimization step increases with the MT length in this scenario making long-running simulations impossible.

To overcome this limitation, we will explore two possibilities to avoid having a MT length-dependent number of minimization parameters:

1. restricting the number of minimization steps per energy minimization to a small value but still considering all minimization parameters (this approach is similar to the strategy in [15]),
2. restricting the number of minimization parameters by only considering the tip of the MT but not restricting the number of minimization steps.

While the first strategy is easy to understand and implement, the second needs further specifications in terms of how we define the tip of the MT here. If a certain event is executed that affects tubulin dimer $(p, d)$, we include all layers starting from $\min(0, d - d_{\mathrm{cutoff}})$ in the mechanical energy minimization because mechanical interactions within the MT have a certain range; $d_{\mathrm{cutoff}}$ is a cutoff *layer* distance (see **Figure 2B**).

Below, we will compare these approaches of restricted minimization with respect to accuracy and speed and find that we obtain accurate energy minimization at a high simulation speed by using the second approach and restricting the number of minimization parameters with $d_{\mathrm{cutoff}} = 10$. We can compare with the approaches of Zakharov et al. [18] and VanBuren et

al. [15] in terms of the average number of minimization steps between chemical events.

Zakharov et al. [18] use $\mathcal{O}(10^7)$ Brownian dynamics steps between events and restrict the number of simulation parameters to 300 tubulin dimers at the plus end. With $d_{\mathrm{cutoff}} = 10$ we minimize on average with respect to a comparable number of 150 tubulin dimers at the plus end. To compare the efficiency, we consider a single quasi-Newton minimization step in our simulation to be equivalent to one time step of their Brownian dynamics (if we ignore the random thermal fluctuations in their Langevin equations, they are basically using a gradient descent method). We compare our event time $t_i$ divided by the number of minimization steps after the execution of that event to their Brownian dynamics time step of $2 \times 10^{-10}$ s. For shrinking MTs, one minimization step takes $\mathcal{O}(10^{-5}\,s)$ after polymerization events, $\mathcal{O}(10^{-4}\,s)$ after depolymerization events, and $\mathcal{O}(10^{-7}\,s)$ after lateral bond events; all of these time steps are orders of magnitude larger than $2 \times 10^{-10}$ s and, thus, the simulation proceeds orders of magnitude faster, while we still achieve an accurate energy minimization. As a comparison with the 1 s of MT dynamics simulated in more than a day in a parallel computation in reference [18], we generally do not require more than a few hours for 1 min of MT dynamics (for a constant hydrolysis rate) using just a single CPU core.

VanBuren et al. [15] apply a local minimization procedure and restrict minimization to, on average, three minimizations with respect to the parameters of each dimer. Because one step of their algorithm minimizes with respect to the parameters of a single tubulin dimer, a comparison to our quasi-Newton minimization steps which minimize the MT energy with respect to the parameters of, on average, $\mathcal{O}(150)$ tubulin dimers is not straightforward. In addition, VanBuren et al.'s model also contains longitudinal springs so that outward bending of single tubulin dimers as a consequence of local minimization can be compensated by stretching the next longitudinal spring. As our model does not contain such longitudinal springs, bending one tubulin dimer causes the whole protofilament part above the tubulin dimer to also bend outwards creating an effectively non-local, far-reaching interaction. Consequently, we are not able to also implement a local minimization procedure for comparison. To make a qualitative comparison between the two approaches, we assume that one minimization step of our BFGS algorithm, which acts on average on 300 parameters, i.e., 150 tubulin dimers, corresponds to 100 single tubulin dimer minimizations in the model of reference [15] as they consider three parameters per tubulin dimer. Between chemical events, we perform on average 150 BFGS minimization steps, which corresponds to $1.5 \times 10^4$ single tubulin dimer minimizations in reference [15]. Therefore, we apply the equivalent of $15,000/150 = 100$ single tubulin minimizations to each of the 150 tubulin dimers close to the plus tip on average as compared to three single tubulin dimer minimizations in the simulation model of reference [15]. Accordingly, we should achieve a more accurate mechanical energy relaxation.

We also compared our chosen minimization method, the BFGS algorithm, against the other multidimensional minimization algorithms using derivatives provided by GSL [53],

including the conjugate gradient method, and found the BFGS algorithm to perform better. In particular, to fully minimize the initial configuration of a MT with $N_{\text{GDP}} = 20$ and $N_{\text{GTP}} = 0$, BFGS only required about a third of the time compared to the next best algorithm, a conjugate gradient method.
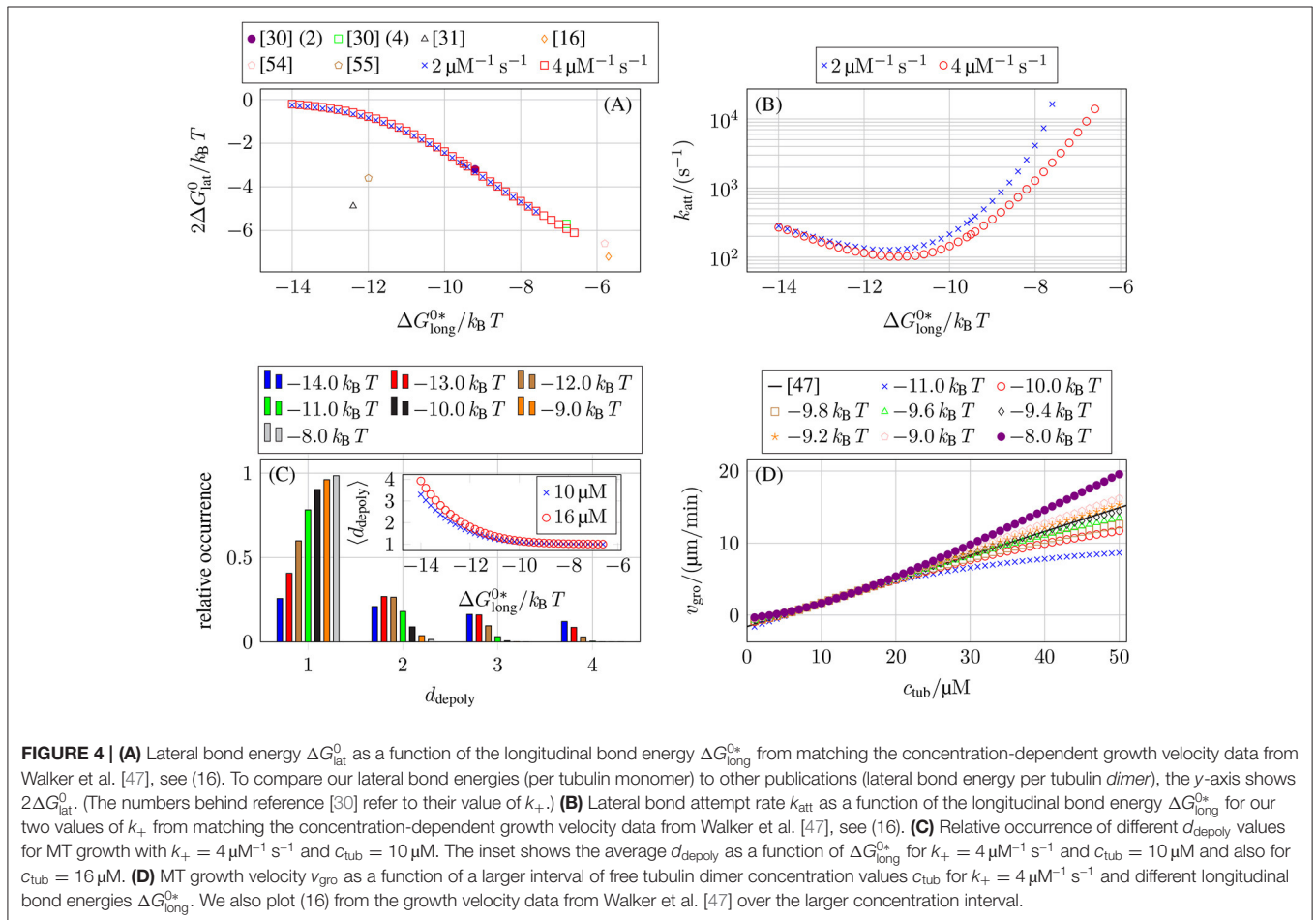
# 3. RESULTS

## 3.1. GTP-Microtubule Growth and Model Parameterization

MT growth mainly depends on the four parameters $k_+$, $\Delta G_{\text{long}}^{0*}$, $\Delta G_{\text{lat}}^0$, and $k_{\text{att}}$, because the growing MT tip mainly consists of straight GTP-tubulin dimers. Therefore, we consider growth of a GTP-only MT ($N_{\text{GDP}} = 0$) in the absence of hydrolysis and set $k_{\text{lat}} = 0$ and $\kappa = 0$ so that the only free parameters left are $k_+$, $\Delta G_{\text{long}}^{0*}$, $\Delta G_{\text{lat}}^0$, and $k_{\text{att}}$. For $k_+ = 2\,\mu M^{-1}\,s^{-1}$ and $k_+ = 4\,\mu M^{-1}\,s^{-1}$, we scanned the parameter space ($\Delta G_{\text{long}}^{0*}, \Delta G_{\text{lat}}^0, k_{\text{att}}$) in steps $\Delta\Delta G_{\text{long}}^{0*} = 0.2\,k_{\text{B}}T$ to find parameter values that reproduce the experimental growth velocity data of Walker et al. in (16). The growth velocity $v_{\text{gro}}$ for each simulation was determined by fitting $\ell_{\text{MT}}(t_{\text{sim}})$ with a linear function. Experiments on MT growth show a linear

dependence $v_{\text{gro}}(c_{\text{tub}}) = a_{\text{gro}}c_{\text{tub}} + b_{\text{gro}}$ characterized by two parameters $a_{\text{gro}}$ and $b_{\text{gro}}$ from (16). If simulations reproduce a linear dependence of $v_{\text{gro}}$ as a function of $c_{\text{tub}}$, we can determine two of the three model parameters ($\Delta G_{\text{long}}^{0*}, \Delta G_{\text{lat}}^0, k_{\text{att}}$) by fitting to the experimental data (16) for $a_{\text{gro}}$ and $b_{\text{gro}}$, i.e., two experimental constraints fix two model parameters as a function of the third parameter. This will allow us to parameterize a one-dimensional sub-manifold (a line) within the three-dimensional parameter space ($\Delta G_{\text{long}}^{0*}, \Delta G_{\text{lat}}^0, k_{\text{att}}$) where our model agrees with experimental growth data. This procedure is conceptually analogous to the approach of VanBuren et al. [30], but we work in a higher-dimensional (three-dimensional) space of model parameters.

As a result, we obtain a line in the three-dimensional parameter space, which we parameterize by $\Delta G_{\text{long}}^{0*}$, i.e., for a given value of $\Delta G_{\text{long}}^{0*}$, a value of $\Delta G_{\text{lat}}^0$ (see **Figure 4A**) and a value of $k_{\text{att}}$ (see **Figure 4B**) is determined by the experimental growth data.

Afterwards, we will fix a particular value of $\Delta G_{\text{long}}^{0*}$ by the additional requirement that the simulation should exhibit an as linear as possible concentration dependence of the growth velocity $v_{\text{gro}}$ over a certain range of tubulin concentrations $c_{\text{tub}}$ (see **Figure 4D**) such that we arrive at parameter sets



**FIGURE 4 | (A)** Lateral bond energy $\Delta G_{\text{lat}}^0$ as a function of the longitudinal bond energy $\Delta G_{\text{long}}^{0*}$ from matching the concentration-dependent growth velocity data from Walker et al. [47], see (16). To compare our lateral bond energies (per tubulin monomer) to other publications (lateral bond energy per tubulin *dimer*), the $y$-axis shows $2\Delta G_{\text{lat}}^0$. (The numbers behind reference [30] refer to their value of $k_+$.) **(B)** Lateral bond attempt rate $k_{\text{att}}$ as a function of the longitudinal bond energy $\Delta G_{\text{long}}^{0*}$ for our two values of $k_+$ from matching the concentration-dependent growth velocity data from Walker et al. [47], see (16). **(C)** Relative occurrence of different $d_{\text{depoly}}$ values for MT growth with $k_+ = 4\,\mu M^{-1}\,s^{-1}$ and $c_{\text{tub}} = 10\,\mu M$. The inset shows the average $d_{\text{depoly}}$ as a function of $\Delta G_{\text{long}}^{0*}$ for $k_+ = 4\,\mu M^{-1}\,s^{-1}$ and also for $c_{\text{tub}} = 16\,\mu M$. **(D)** MT growth velocity $v_{\text{gro}}$ as a function of a larger interval of free tubulin dimer concentration values $c_{\text{tub}}$ for $k_+ = 4\,\mu M^{-1}\,s^{-1}$ and different longitudinal bond energies $\Delta G_{\text{long}}^{0*}$. We also plot (16) from the growth velocity data from Walker et al. [47] over the larger concentration interval.

$(\Delta G_{\text{long}}^{0*}, \Delta G_{\text{lat}}^{0}, k_{\text{att}})$ for $k_+ = 2\,\mu M^{-1}\,s^{-1}$ and $k_+ = 4\,\mu M^{-1}\,s^{-1}$ (see **Table 3**).

The results in **Figure 4A** show that the values of $\Delta G_{\text{long}}^{0*}$ and $\Delta G_{\text{lat}}^{0}$ depend only weakly on our chosen $k_+$ values. **Figure 4A** also shows that our data matches results obtained in [30] (this data was later re-used in [15, 16, 54]) but also differs from other results [31, 55], which were all obtained by the same approach of fitting growth velocity data from Walker et al. [47] (or their own growth data in [55]). Kononova et al. [43] obtained bond energies from MD simulations of nano-indentation experiments; the values from Kononova et al. [43] are much larger for both types of bonds ($\Delta G_{\text{long}}^{0*} \sim 2\Delta G_{\text{lat}}^{0} \sim 25 k_B T$) and, thus, not shown in **Figure 4A**.

Qualitatively, the measured dependencies of $\Delta G_{\text{lat}}^{0}$ and $k_{\text{att}}$ on $\Delta G_{\text{long}}^{0*}$ can be understood as follows: the weaker longitudinal bonds are, the more likely it is that a tubulin dimer will depolymerize. To get the same growth velocity, this decrease in "longitudinal stability" has to be compensated by an increase in "lateral stability" by stronger lateral bonds (making it less likely that lateral bonds break and, thus, enabling depolymerization) or faster formation of lateral bonds (to stabilize newly polymerized tubulin dimers). **Figure 4C** shows the number of tubulin dimers $d_{\text{depoly}}$ that detach at once during depolymerization events. For increasingly stronger longitudinal bonds and, thus, weaker lateral bonds, multi-dimer depolymerization becomes more relevant. The data in the inset in **Figure 4C** is also compatible with results in reference [33] obtained with a purely chemical model.

Until now, we only considered free tubulin dimer concentrations $c_{\text{tub}} \in [7, 16\,\mu M]$ to use similar values as Walker et al. [47], but there have also been other measurements with a larger range of $c_{\text{tub}}$ values [3, 48, 51, 52]. In general, it is assumed that the growth velocity $v_{\text{gro}}$ increases linearly with $c_{\text{tub}}$ for the whole MT just as the polymerization rate in (7) increases linearly with $c_{\text{tub}}$ for individual protofilaments. Theoretically, it has been shown that, for multistranded polymers, lateral interactions give rise to a non-linear relation between growth velocity on monomer concentration [56]. For MT growth, a non-linear dependence on tubulin concentration was found in reference [31] using a two-dimensional model based on reference [30]. Over a larger range of $c_{\text{tub}}$ values, our simulations also exhibit a non-linear relation between $v_{\text{gro}}$ and $c_{\text{tub}}$ depending on the value of $\Delta G_{\text{long}}^{0*}$, as shown in **Figure 4D**. Data for different values of $\Delta G_{\text{long}}^{0*}$ (and correspondingly adjusted values of $\Delta G_{\text{lat}}^{0}$ and $k_{\text{att}}$, see **Figures 4A,B**) and the same value of $k_+$ that was previously overlapping in the interval $c_{\text{tub}} \in [7, 16\,\mu M]$ start to differentiate in a larger concentration interval. While possible

non-linear relations have been predicted theoretically, the available experimental data show a linear $v_{\text{gro}}(c_{\text{tub}})$ dependence over a large range of $c_{\text{tub}}$ values [3, 48, 51, 52]. Therefore, we determined the remaining free parameter value of $\Delta G_{\text{long}}^{0*}$ for the two $k_+$ values from the condition that the concentration dependence of $v_{\text{gro}}$ is as linear as possible up to 50 $\mu$M. To determine these values of $\Delta G_{\text{long}}^{0*}$, we ignored concentrations $c_{\text{tub}}$ below the individual critical concentration (for which $v_{\text{gro}} < 0$) which violate our fundamental assumption of a growing MT.

In summary, we find a triple $(\Delta G_{\text{long}}^{0*}, \Delta G_{\text{lat}}^{0}, k_{\text{att}})$ that fits the growth velocity data from Walker et al. [47] and that gives a linear concentration dependence over a wide tubulin concentration range for two representative values of $k_+$. **Table 3** lists these parameter triples for $k_+ = 2\,\mu M^{-1}\,s^{-1}$ and $k_+ = 4\,\mu M^{-1}\,s^{-1}$. For a given $k_+$, these results fix four of the seven model parameters in **Table 2** using experimental data on MT growth. To address the parameters $\kappa$ and $k_{\text{lat}}$, we now turn to MT shrinkage.

## 3.2. GDP-Microtubule Shrinkage and Model Parameterization

As opposed to MT growth, MT shrinkage also depends on the bending constant $\kappa$ and spring constant $k_{\text{lat}}$ as protofilament curling and bond rupture become relevant processes for a shrinking MT. We consider a shrinking MT that initially only consists of GDP-tubulin dimers ($N_{\text{GTP}} = 0$, $N_{\text{GDP}} > 0$) with parameter values $k_+$, $\Delta G_{\text{long}}^{0*}$, $\Delta G_{\text{lat}}^{0}$, and $k_{\text{att}}$ as already determined by the growth simulations and in the absence of hydrolysis (a shrinking, initially GDP-only MT acquires some GTP-dimers by attachment but remains GDP-dominated). To investigate shrinkage, MTs with $N_{\text{GDP}} = 20$ and $N_{\text{GTP}} = 0$ were used. For each parameter set, 20 simulations were run to get an average shrinkage velocity $v_{\text{shr}}$. Experimental data on shrinking MTs show a shrinkage speed $v_{\text{shr}}$ that is independent of the tubulin dimer concentration. For each value of $k_+$, we should be able to determine one of the two parameters ($\kappa, k_{\text{lat}}$) as a function of the other parameter by fitting such that the experimental value of the shrinkage velocity is reproduced in simulations (for parameters $\Delta G_{\text{long}}^{0*}$, $\Delta G_{\text{lat}}^{0}$, and $k_{\text{att}}$ fixed by the growth velocity data). We use the experimental shrinkage velocity of Walker et al., see (17), for this fitting procedure.

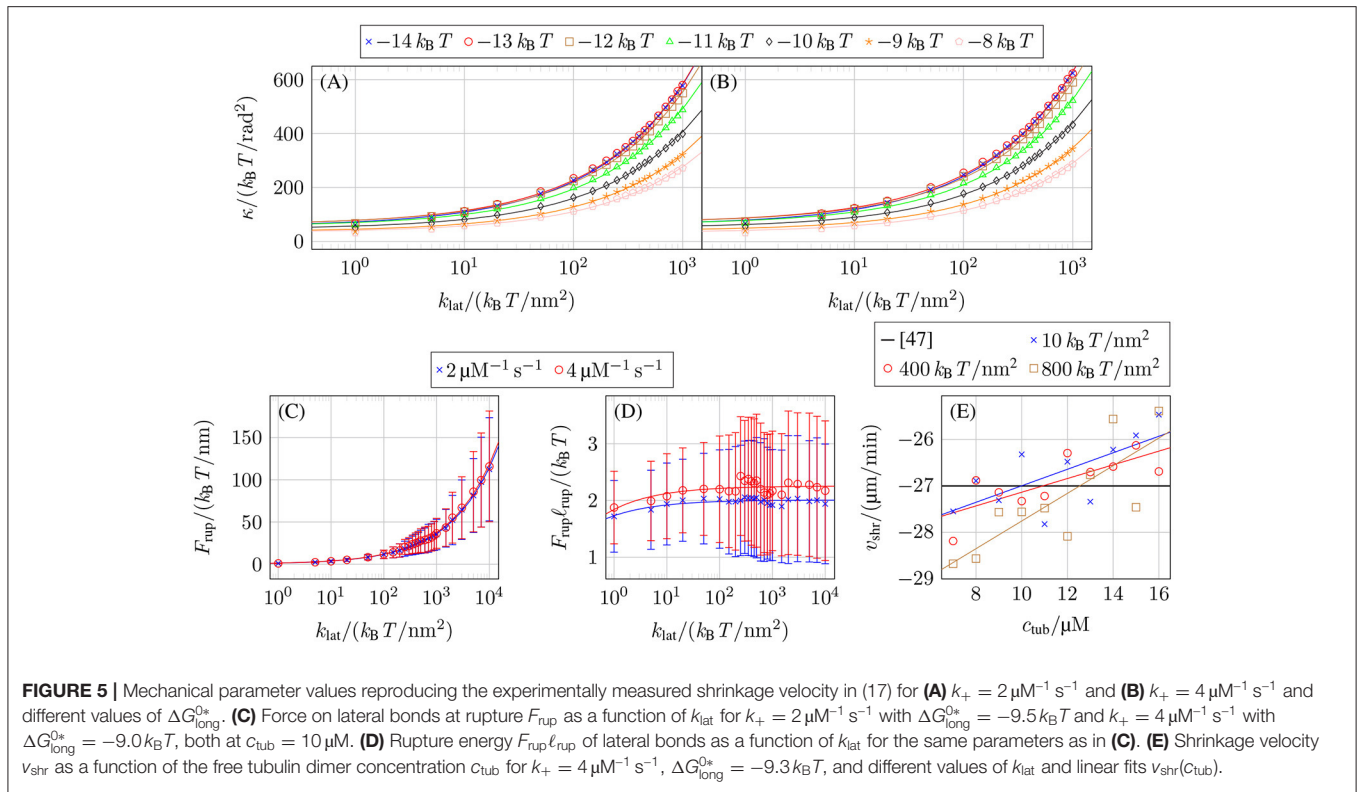**Figures 5A,B** show the values of $k_{\text{lat}}$ and $\kappa$ for $k_+ = 2\,\mu M^{-1}\,s^{-1}$ and $k_+ = 4\,\mu M^{-1}\,s^{-1}$ and different values of $\Delta G_{\text{long}}^{0*}$ that reproduce the experimentally measured shrinkage velocity in (17). All data points for each $\Delta G_{\text{long}}^{0*}$ fall on square root functions

$$\kappa(k_{\text{lat}}) = a_{\text{shr}}\sqrt{k_{\text{lat}}} + b_{\text{shr}}. \tag{18}$$

This functional dependence can be understood qualitatively by considering the mechanical contribution to the bond rupture rate (10), $\exp(F_{\text{lat}}\ell_{\text{rup}})$, which, on average, should have the same value for all mechanical parameter combinations to produce the same shrinkage velocity. As the characteristic bond rupture length in (11) depends on $k_{\text{lat}}$ as $\ell_{\text{rup}} \sim \sqrt{k_{\text{lat}}}^{-1}$, the average lateral bond force at rupture should depend on $k_{\text{lat}}$ like $F_{\text{rup}} \sim k_{\text{lat}}\ell_{\text{rup}} \sim$

**TABLE 3 |** Growth parameter values that generate the most linear dependence $v_{\text{gro}}(c_{\text{tub}})$.

| $k_+$ ($\mu M^{-1}\,s^{-1}$) | 2 | 4 |
|---|---|---|
| $\Delta G_{\text{long}}^{0*}$ ($k_B T$) | −9.7 | −9.3 |
| $\Delta G_{\text{lat}}^{0}$ ($k_B T$) | −1.38 | −1.58 |
| $k_{\text{att}}$ ($s^{-1}$) | 281 | 258 |

**FIGURE 5** | Mechanical parameter values reproducing the experimentally measured shrinkage velocity in (17) for **(A)** $k_+ = 2\,\mu M^{-1}\,s^{-1}$ and **(B)** $k_+ = 4\,\mu M^{-1}\,s^{-1}$ and different values of $\Delta G_{long}^{0*}$. **(C)** Force on lateral bonds at rupture $F_{rup}$ as a function of $k_{lat}$ for $k_+ = 2\,\mu M^{-1}\,s^{-1}$ with $\Delta G_{long}^{0*} = -9.5\,k_B T$ and $k_+ = 4\,\mu M^{-1}\,s^{-1}$ with $\Delta G_{long}^{0*} = -9.0\,k_B T$, both at $c_{tub} = 10\,\mu M$. **(D)** Rupture energy $F_{rup}\ell_{rup}$ of lateral bonds as a function of $k_{lat}$ for the same parameters as in **(C)**. **(E)** Shrinkage velocity $v_{shr}$ as a function of the free tubulin dimer concentration $c_{tub}$ for $k_+ = 4\,\mu M^{-1}\,s^{-1}$, $\Delta G_{long}^{0*} = -9.3\,k_B T$, and different values of $k_{lat}$ and linear fits $v_{shr}(c_{tub})$.

$\sqrt{k_{lat}}$. The lateral bond force $F_{lat}$ is a consequence of the lateral bonds stretching as the tubulin monomers curl outward to decrease the bending force $F_{bend} = \kappa \left( \Delta\theta(p,d,t) - \Delta\theta_0(p,d,t) \right)$, which leads to $F_{rup} \sim F_{bend} \sim \kappa$ resulting in $\kappa \sim \sqrt{k_{lat}}$ in accordance with **Figures 5A,B**.

**Figure 5C** confirms that the average force on lateral bonds at rupture $\langle F_{rup} \rangle$ has the functional dependence $\langle F_{rup} \rangle \sim \sqrt{k_{lat}}$ predicted by our above qualitative argument ($\langle F_{rup} \rangle$ and error bars $\sigma_{F_{rup}}$ were determined by fitting normal distributions to the histogram of the lateral bond rupture forces collected for 20 shrinkage simulations per parameter set with $N_{GDP} = 20$). Also, the resulting mechanical contribution $F_{rup}\ell_{rup}$ for the exponential function of the lateral bond rupture rate in **Figure 5D** is approximately constant as expected from our above argument.
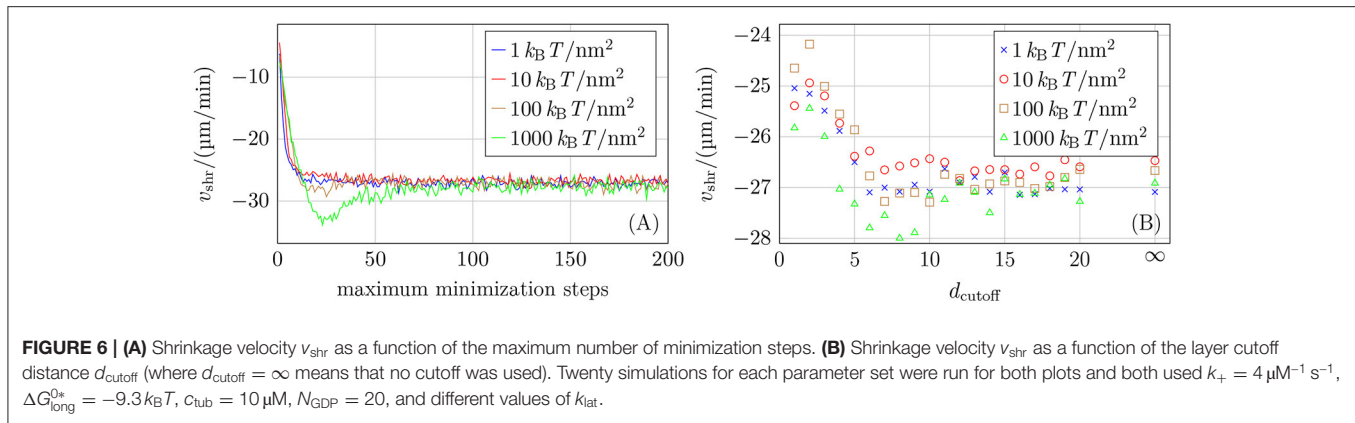
As the experimentally measured shrinkage velocity $v_{shr}$ does not depend on the free tubulin dimer concentration $c_{tub}$, we used constants to fit our $v_{shr}(c_{tub})$ data. In reality, however, our data shows a linear dependence between $v_{shr}$ and $c_{tub}$ as shown in **Figure 5E** corresponding to a slowing down of depolymerization. This is caused by an increased probability for intermediate addition of tubulin dimers and lateral bond formation between them; these lateral bonds require additional time to rupture. While this dependency of $v_{shr}$ on $c_{tub}$ will have a small influence on the concrete value of the shrinkage velocity, we expect it to not have any qualitative effect on the overall MT dynamics. At higher tubulin concentrations, where the decrease of $|v_{shr}(c_{tub})|$ would become significant, the catastrophe rates decrease dramatically so that shrinking will rarely occur.

Comparing our results from **Figures 5A,B** to other results is not always directly possible due to different modeling approaches but most find that $k_{lat} \ll 1.000\,k_B T/nm^2$ and $\kappa \ll 1.000\,k_B T/rad^2$ [15, 57, 58], with some exceptions [43, 59]. Previously, we used MD simulation data from Grafmüller et al. [60] to calculate the bending constant $\kappa$ [17]. Compared to reference [17], we have to adjust the calculation to consider both inter-dimer and intra-dimer bending resulting in $\kappa \simeq 50\,k_B T/rad^2$. MD simulation in Kononova et al. [43], on the other hand, give a persistence length of individual protofilaments of $L_p \simeq 6\,\mu m$, which corresponds to a significantly larger value of $\kappa \simeq 1.500\,k_B T/rad^2$ for the bending constant. This discrepancy cannot be resolved at present. We use $\kappa = 149\,k_B T/rad^2$ in the following together with the corresponding value of $k_{lat} = 100\,k_B T/nm^2$ according to **Figure 5B** which are values close to the ones used by VanBuren et al. [15].

## 3.3. Restricted Energy Minimization for Efficient Simulation

Until now, energy minimization was not restricted by either a maximum number of minimization steps or by only considering a subset of tubulin dimers at the MT tip so that we will consider this unrestricted minimization as the "gold standard" to which we will compare the two restricted energy minimization approaches described in section 2.4. We use the shrinkage velocity $v_{shr}$ as the observable by which we judge the relevant cutoff values in the two approaches.

For restricting the number of quasi-Newton minimization steps, **Figure 6A** shows that an acceptable maximum number of

**FIGURE 6 | (A)** Shrinkage velocity $v_{\text{shr}}$ as a function of the maximum number of minimization steps. **(B)** Shrinkage velocity $v_{\text{shr}}$ as a function of the layer cutoff distance $d_{\text{cutoff}}$ (where $d_{\text{cutoff}} = \infty$ means that no cutoff was used). Twenty simulations for each parameter set were run for both plots and both used $k_+ = 4\,\mu M^{-1}\,s^{-1}$, $\Delta G_{\text{long}}^{0*} = -9.3\,k_B T$, $c_{\text{tub}} = 10\,\mu M$, $N_{\text{GDP}} = 20$, and different values of $k_{\text{lat}}$.

minimization steps reproducing $v_{\text{shr}} = -27\,\mu m/min$ depends on the chosen mechanical parameters as the higher their values are, the greater the energy and its gradient. A maximum number of minimization steps of around 100 should be an appropriate value according to the results shown in **Figure 6A**. The results in **Figure 6A** also show that reducing the number of minimization steps by a factor of 10 can lead to deviating growth velocities. Therefore, the improved energy relaxation that we obtain in comparison to reference [15] by applying the equivalent of one order of magnitude more minimization steps should be relevant.

If minimization is restricted to a subset of minimization parameters at the tip of the simulated MT, this subset is defined by the cutoff distance $d_{\text{cutoff}}$. To have a maximum improvement in simulation speed, $d_{\text{cutoff}}$ should be as small as possible. It is evident from the data shown in **Figure 6B** that values $d_{\text{cutoff}} < 5$ have a detectable influence on the shrinkage velocity. We also ran some simulations with $N_{\text{GDP}} = 50$ and also for $k_+ = 2\,\mu M^{-1}\,s^{-1}$ (see **Figure S8** in the Supplementary Material) and based on all data, we choose $d_{\text{cutoff}} = 10$ as a conservative value for the cutoff distance.

In summary, we are more confident in the second approach to only minimize the MT tip where actual conformational changes happen, because for this subset, the restricted energy is fully minimized. Additionally, the first approach still has the issue of slowing down with an increasing number of minimization parameters as all minimization parameters are considered. The second approach ensures that the number of minimization parameters does not scale with the MT length but remains bounded, which assures that we can simulate arbitrarily long growing MTs at a fixed minimal computational speed. In the first approach, the quality of the minimization will probably also decline because the number of minimization parameters increases while the number of minimization steps is kept constant. Lastly, the first approach, in contrast to the second approach, does not guarantee that the upper, i.e., the dynamic part of the MT is properly minimized.

We also note that in the presence of mechanical feedback onto hydrolysis, simulations take longer because minimizations after hydrolysis events need to consider more tubulin dimers if the hydrolyzed tubulin dimer is relatively deep in the MT lattice (see **Supplementary Material** for more details).

## 3.4. Full Simulations Exhibit Repeated Catastrophe and Rescue Events

Based on the previous section on energy minimization, we use $d_{\text{cutoff}} = 10$ for full simulations in which the initial MTs have both a GDP-body and a GTP-cap, thus $N_{\text{GDP}} > 0$ and $N_{\text{GTP}} > 0$. We now aim for realistic MT dynamics with repeated phases of growth and shrinkage in the same simulation and catastrophe and rescue events in between. First, we only consider strictly random hydrolysis with a hydrolysis rate $k_{\text{hydr}}$ that is independent of tubulin dimers' position or mechanical forces and which is another unknown free parameter in our model. Hydrolysis coupled to mechanics via (12) will be considered later.

It poses a computational challenge for chemomechanical MT models to reach time scales of MT dynamics where repeated catastrophe events occur at realistic hydrolysis rates $k_{\text{hydr}}$ and tubulin dimer concentrations $c_{\text{tub}}$. In reference [18], where mechanics was implemented via full Brownian dynamics, only short times scales could be reached (although the Brownian dynamics was applied to only 300 tubulin dimers at the plus end). Therefore, they increased the hydrolysis rate from their "normal" value of $0.5\,s^{-1}$ (based on the $2\,s$ delay between polymerization and phosphate release measured by [61], which is also used by [62]) into a range of $3-11\,s^{-1}$ in order to trigger catastrophe events within computationally accessible time scales. They found a linear scaling of catastrophe rate with $k_{\text{hydr}}$ and employed a linear extrapolation to obtain catastrophe rates for realistic hydrolysis rates (see their Figure 3A). In our simulations, we observe that increasing $k_{\text{hydr}}$ beyond a certain ($c_{\text{tub}}$-dependent) value leads to immediate MT shrinkage because the initial cap quickly hydrolyzes; this can be interpreted as an instantaneous catastrophe. In such cases (like in **Figure 7** for $c_{\text{tub}} = 7\,\mu M$ and $k_{\text{hydr}} = 0.5\,s^{-1}$), there is no real growth phase based on which a catastrophe frequency could be determined. For these hydrolysis rates, the individual critical concentration $c_{\text{tub,c}}$ (where $v_{\text{gro}} = 0$ is reached) has apparently increased above the given tubulin concentration.

The experimental data on the hydrolysis rate is limited, so that many publications determine the hydrolysis rate themselves by matching simulation results with experimental data [16, 30–33, 63–65]. There are, however, more direct measurements in
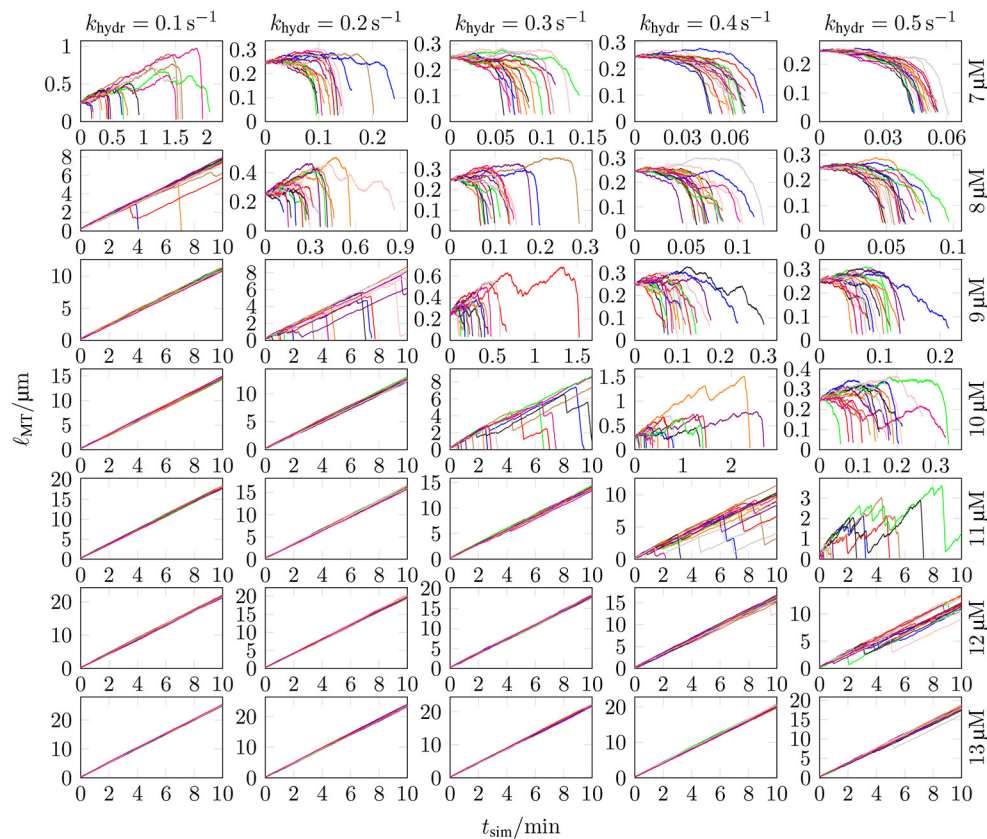
**FIGURE 7 |** The MT length $\ell_{MT}$ was measured as a function of the simulation time $t_{sim}$ for 20 different simulations with $k_+ = 4\,\mu M^{-1}\,s^{-1}$, $\Delta G^{0*}_{long} = -9.3\,k_B T$, $k_{lat} = 100\,k_B T/nm^2$, seven different values of $c_{tub}$, and five different values of $k_{hydr}$. MT growth trajectories for three additional $c_{tub}$ values can be found in **Figure S9** in the Supplementary Material.

Melki et al. [61]. In most models and also in measurements from Melki et al. [61], the (random) hydrolysis rate is in the range of $0.1$–$0.5\,s^{-1}$ (reference [30] use a relatively high value of $0.95\,s^{-1}$). We explore exactly this range of hydrolysis rates, see **Figure 7**.

**Figure 7** shows MT growth curves (length vs. time) over simulation times up to $t_{sim} = 10$ min for several representative tubulin concentrations and realistic hydrolysis rates. MT growth trajectories as in **Figure 7** for other $k_{lat}$ values can be found in **Figures S10–13** in the Supplementary Material. Simulations in **Figure 7** were started with $N_{GTP} = 10$ and $N_{GDP} = 20$, but results are largely independent of the initial ratio $N_{GTP}/N_{GDP}$ (see, e.g., **Figure S11** in the Supplementary Material).

Our chemomechanical MT model is computationally efficient such that we can determine catastrophe and rescue rates as inverse average growth and shrinking times between repeated catastrophe and rescue events. In the **Supplementary Material**, we explain the algorithm that we used to identify catastrophe and rescue events and, thus, growth and shrinking times from MT simulation trajectories in detail. The results are shown in **Figure 8**. In comparison to typical experimental data [47, 67], the decrease of the catastrophe rate with tubulin concentration seems too steep. Current phenomenological models for the MT

catastrophe rate as a function of tubulin concentration can be found in Flyvbjerg et al. [68] and Zelinski and Kierfeld [69], experimental data in Walker et al. [47] and Janson et al. [66]; the decrease of the catastrophe rate with GTP-tubulin concentration $c_{tub}$ appears steeper in the simulation for all hydrolysis rates $k_{hydr} = 0.1$–$0.5\,s^{-1}$.

In the following, we will discuss two aspects of MT growth and catastrophes in more detail, namely the dependence of growth velocity on hydrolysis rate and the detailed dynamics within single catastrophe events, which become accessible within a computational model and are impossible to address experimentally.

## 3.5. Growth Velocity Reduces Linearly With Hydrolysis Rate Because of Cap Structure

So far, we parameterized the model by fitting the growth velocity of GTP-only MTs, i.e., in the absence of hydrolysis to the experimentally measured velocity in (16). Hydrolysis reduces this growth velocity by increasing the probability of GDP-dimers at the plus end. This increases the rate of bond rupture because hydrolyzed dimers tend to create stretched bonds which rupture more easily (there is no direct increase of the off-rate
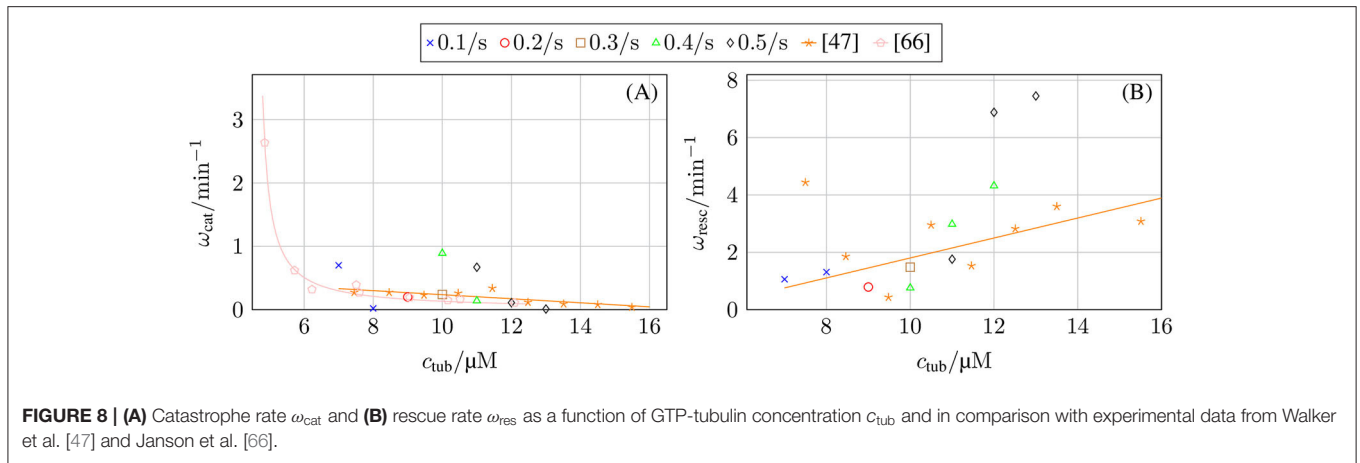
**FIGURE 8 | (A)** Catastrophe rate $\omega_{cat}$ and **(B)** rescue rate $\omega_{res}$ as a function of GTP-tubulin concentration $c_{tub}$ and in comparison with experimental data from Walker et al. [47] and Janson et al. [66].
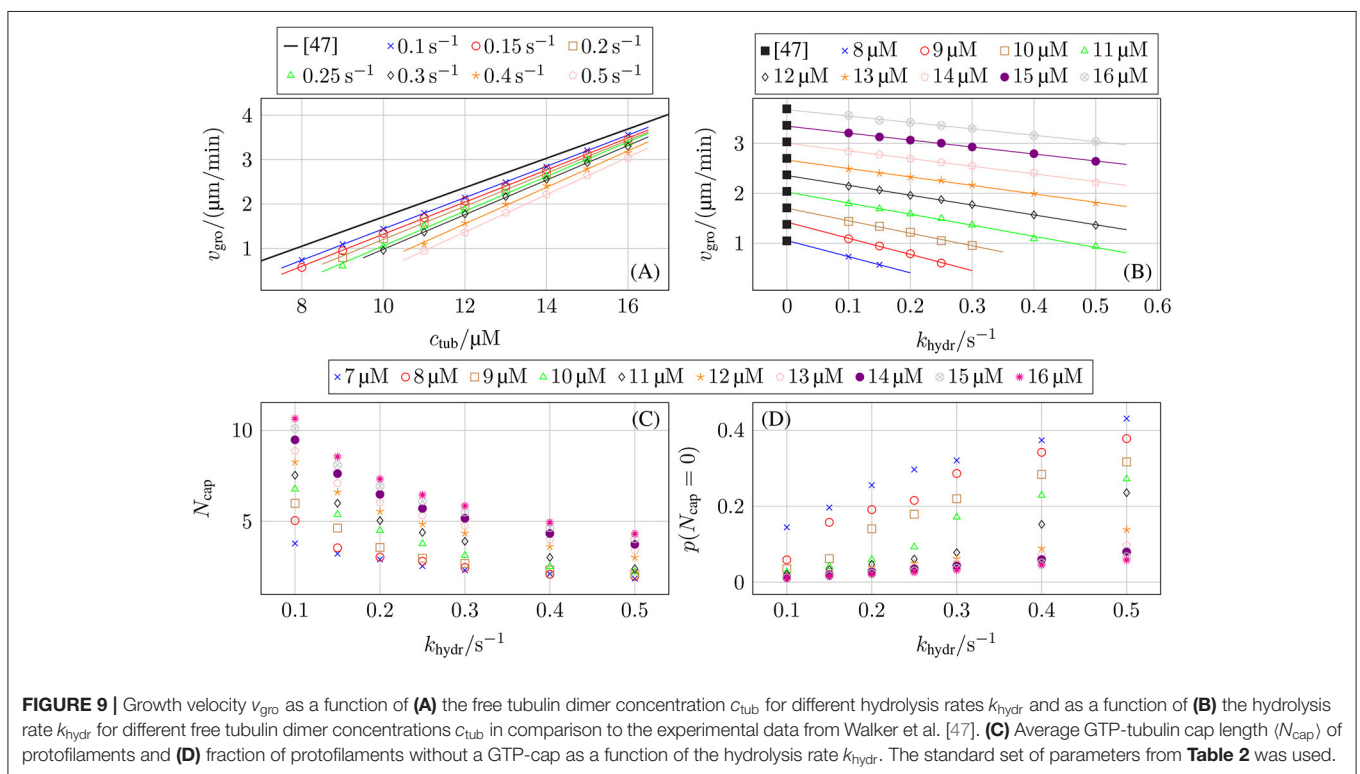


**FIGURE 9 |** Growth velocity $v_{gro}$ as a function of **(A)** the free tubulin dimer concentration $c_{tub}$ for different hydrolysis rates $k_{hydr}$ and as a function of **(B)** the hydrolysis rate $k_{hydr}$ for different free tubulin dimer concentrations $c_{tub}$ in comparison to the experimental data from Walker et al. [47]. **(C)** Average GTP-tubulin cap length $\langle N_{cap} \rangle$ of protofilaments and **(D)** fraction of protofilaments without a GTP-cap as a function of the hydrolysis rate $k_{hydr}$. The standard set of parameters from **Table 2** was used.

for hydrolyzed GDP-dimers in our model). As only laterally unbounded dimers can detach, hydrolyzed GDP-dimers at the plus end have an effectively higher detachment rate.

The last row of **Figure 7** indicates and **Figure 9B** shows explicitly that increasing the hydrolysis rate decreases the growth velocity linearly although the growth reduction mechanism is indirect via the increased probability of bond rupture for hydrolyzed GDP-dimers. Our model parameterization was such that we obtain the experimentally measured growth velocities by Walker et al. [47] at $k_{hydr} = 0\,s^{-1}$ in **Figure 9B**. Nevertheless, **Figure 9A** shows that there is still a linear relation between the free tubulin dimer concentration $c_{tub}$ and the growth velocity $v_{gro}$ so that it is possible to re-adjust parameters to reproduce the

growth velocity in the presence of hydrolysis, once a particular hydrolysis rate can be reliably selected.

Because both the dependence on tubulin concentration in **Figure 9A** remains linear and the reduction by the hydrolysis rate in **Figure 9B** is linear, we also expect that the individual critical concentration (where $v_{gro} = 0$ is reached) increases linearly with the hydrolysis rate beyond the value $c_{tub,c} \simeq 5\,\mu M$ of Walker et al. [47]. **Figure 7** clearly shows that increasing $k_{hydr}$ actually increases the individual critical concentration $c_{tub,c}$.[2]

---

[2]The individual critical concentration can be read off from **Figure 7** as the concentration below which immediate MT shrinkage sets in.
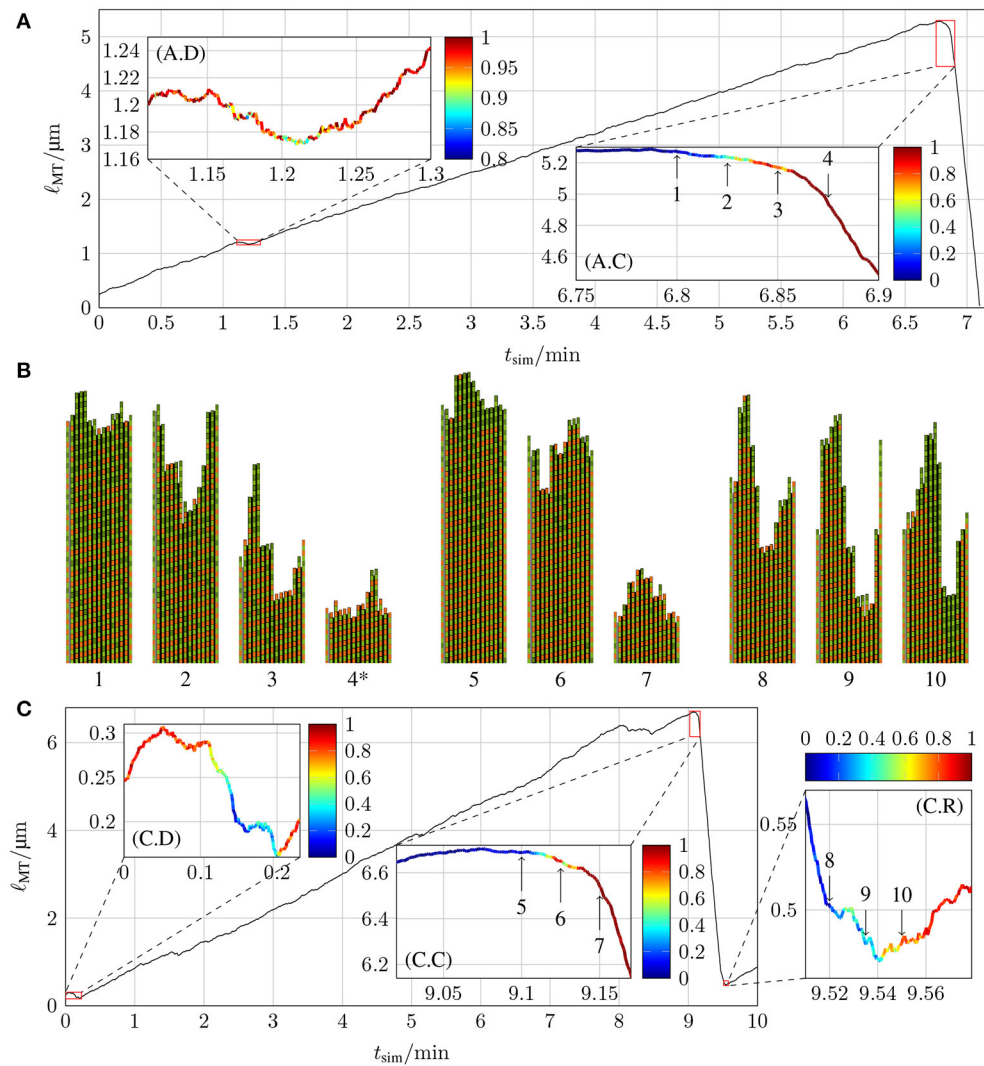
**FIGURE 10 |** Lengths of two MTs as a function of simulation time $t_{\text{sim}}$ with $k_+ = 4\,\mu\text{M}^{-1}\,\text{s}^{-1}$, $\Delta G_{\text{long}}^{0*} = -9.3\,k_{\text{B}}T$, $k_{\text{lat}} = 100\,k_{\text{B}}T/\text{nm}^2$, and **(A)** $c_{\text{tub}} = 8\,\mu\text{M}$ and $k_{\text{hydr}} = 0.1\,\text{s}^{-1}$ and **(C)** $c_{\text{tub}} = 9\,\mu\text{M}$ and $k_{\text{hydr}} = 0.2\,\text{s}^{-1}$. The insets highlight parts of the trajectories of interest for the dynamics and color-code the probability of the $\ell_{\text{MT}}(t_{\text{sim}})$ curve to stay quantitatively the same at the relevant point in time if new simulations are started with the relevant configuration as the initial configuration (for more details, refer to the text). **(B)** shows the two-dimensional representations of certain MT tip configurations that are marked by arrows in the insets of **(A,C)** (configuration 4* has been shifted toward the MT tip by 24 tubulin dimer lengths). The first protofilament is the periodic image of $p = 13$ and the last protofilament is the periodic image of $p = 1$. Lateral bonds are represented by the thick black line between protofilaments.

The mechanism of growth velocity reduction by hydrolysis can be further elucidated by comparing the average GTP-tubulin cap length $\langle N_{\text{cap}} \rangle$ of protofilaments (see **Figure 9C**), and the fraction of protofilaments without a GTP-cap (see **Figure 9D**): The higher the hydrolysis rate is, the smaller the GTP-cap and the higher the fraction of cap-less protofilaments is.[3] The increase in GDP-tubulin dimers depolymerizing from the protofilament tips for higher hydrolysis rates is due to an increase in the probability

of uncapped protofilaments with the hydrolysis rate as shown in **Figure 9D**. In reference [70], dependencies $\langle N_{\text{cap}} \rangle \propto \sqrt{c_{\text{tub}}/k_{\text{hydr}}}$ and $p(N_{\text{cap}} = 0) \propto k_{\text{hydr}}/c_{\text{tub}}$ have been predicted, which are in agreement with **Figures 9C,D**.

## 3.6. Detailed Dynamics Within Single Catastrophe and Rescue Events

The chemomechanical model reproduces realistic MT dynamics including catastrophe and rescue events. **Figure 10** shows typical MT growth paths featuring two catastrophe events and a rescue event in subfigure (C). Moreover, we observe "dips" in the growth path where a short phase of shrinking appears, which are

---

[3] As the cap lengths shown in **Figure 9C** are averaged over the whole duration of the simulations, these cap lengths also average over growth and shrinkage phases. As cap lengths are shorter during shrinkage than growth, the cap lengths in **Figure 9C** can be regarded as a lower limit on the average cap length during MT growth.

similar to "stutter" events that have been observed in reference [35]. Videos of these two simulations with two- and three-dimensional representations of the MT structure can be found in the **Supplementary Material**.

Using our computational model, we can systematically identify the point in a MT growth path, where a catastrophe becomes structurally unavoidable. This allows us to search for typical catastrophe-triggering features in MT growth. To analyze how probable it is at specific points in the simulation of MT dynamics that the MT continues a certain growth path, we chose two simulations with at least one significant event (meaning a catastrophe, rescue, or a "dip"/"stutter") and took configurations around such events as starting points for new simulations (similar to [33]). In these new simulations, MTs were allowed to grow (or shrink) for a maximum of 60 s, a sufficient amount of time to check if the new simulations show dynamics similar to the original simulation around the significant event.

The MT growth trajectory shown in **Figure 10A** has two significant events: a dip at $t_{\text{sim}} = 1.2\,min$ and a catastrophe at $t_{\text{sim}} = 6.85\,min$; the trajectory in **Figure 10C** contains three significant events: a dip at the very beginning, a catastrophe at $t_{\text{sim}} = 9.15\,min$, and a rescue at $t_{\text{sim}} = 9.54\,min$. To determine whether newly run simulations with starting points from the initial simulation qualitatively follow the original simulation, we need criteria to identify dips, catastrophes, or rescue events. The exact criteria for these events in **Figures 10A,C** are stated in the **Supplementary Material**. In short, in order to identify whether a new simulation reproduces a catastrophe, we check after a time of 10–15 s whether the MT is sufficiently short that a catastrophe must have happened; for a dip, we check whether the MT continued to grow without entering a catastrophe; for a rescue, we check that the MT did not completely vanish because it continued to shrink. For each initial configuration, we ran 20 new simulations and calculated the fraction of simulations that fulfilled these criteria. These fractions are the probabilities for the original growth path at different points in time, and they are shown color-coded in all the insets in **Figure 10**.

Both catastrophes and the rescue show that the transition from a high probability to stay in the current dynamic state to a high probability to switch into the other dynamic state occurs within a few seconds. In **Figures 10A,C**, we first observe that catastrophes become practically unavoidable [red color code in (A.C) and (C.C)] after a phase of relatively slow shrinking by 50–100 nm; similar "transitional catastrophe" behavior has been observed in reference [35]. A dip, on the other hand, can only evade a catastrophe [yellow to red color code in (A.D) and (C.D)] if the MT length shrinks by significantly $< 50\,nm$.

Because hydrolysis followed by straining and rupture of the lateral bonds is required before a laterally unbonded dimer can detach, MT shrinking by $50\,nm$ suggests that roughly 6 dimer layers must hydrolyze in a row to trigger a catastrophe. This is, however, not sufficient to remove the entire GTP-cap. The GTP-cap length averaged over all protofilaments is still $> 1$ when the catastrophe becomes unavoidable (at points 3 in **Figure 10A** and 6 in **Figure 10C**, see also **Figure S1** in the Supplementary Material). As the corresponding MT snapshot insets 3 and 6 reveal, the reason for this discrepancy is the average over all protofilaments: it appears that typically only a "nucleus" of

three neighboring protofilaments shrinks by more than 6 dimers, such that its GTP-cap is removed and its ends reach into the GDP-body of the MT, when a catastrophe is triggered. The MT snapshots in **Figure 10B** also suggest that rescue events require formation of a GTP-cap on almost all 13 protofilaments (with an average cap length $\sim 4$) such that nuclei of three neighboring uncapped GDP-protofilaments are avoided. Further investigation of more catastrophe events will be necessary to definitely deduce catastrophe- and rescue-triggering structural MT features.

## 3.7. Hydrolysis Coupled to Mechanics Changes the Cap Structure

We also test how a mechanical feedback onto the hydrolysis rate as introduced in (12) and (14) changes the cap structure and dynamic behavior. In the presence of this mechanical feedback, tubulin dimers in the MT lattice with larger bending angles tend to hydrolyze preferentially.

Overall, we find a linear relation between $k_{\text{hydr}}^0$ and the average hydrolysis rate $\langle k_{\text{hydr}} \rangle$ (see **Figure 11A**) with $k_{\text{hydr}}^0 \gg \langle k_{\text{hydr}} \rangle$. When comparing MT growth with hydrolysis coupled to mechanics with average hydrolysis rate $\langle k_{\text{hydr}} \rangle$ to MT growth with constant hydrolysis rate $k_{\text{hydr}}$ (for example in **Figures 11D–F**), we use **Figure 11A** to choose the base hydrolysis rate $k_{\text{hydr}}^0$ such that $\langle k_{\text{hydr}} \rangle \approx k_{\text{hydr}}$.

**Figure 11B** shows the average hydrolysis rate $\langle k_{\text{hydr}} \rangle$ as a function of the free tubulin dimer concentration $c_{\text{tub}}$ for $k_{\text{hydr}}^0 = 1.5\,s^{-1}$. Here, we observe a pronounced non-linear concentration dependence with a decrease around the individual critical tubulin concentration $c_{\text{tub}} \simeq 10\,\mu M$. At the same concentration, also the porous cap length $N_{\text{pcap}}$ (see **Figure 11C**), which is defined as the difference between the number of tubulin dimers in a protofilament and the value of $d$ of the first GTP-tubulin dimer counted from the minus end, starts to increase. As a result, the porous cap length for hydrolysis coupled to mechanics is much longer compared to a constant hydrolysis rate, even if the average effective hydrolysis rate is roughly the same. In the following, we argue that the reason for this increase in porous cap length is a decrease of the hydrolysis rate for GTP-dimers away from the tip. Mechanical feedback gives rise to preferential hydrolysis at the tip, i.e., the average hydrolysis rate $\langle k_{\text{hydr}}(x) \rangle$ (over all actually executed hydrolysis events) is larger for small layer distances $x \equiv d(p) - d$ from the tip, as can be seen in **Figure 11G**. This is in line with previous results in reference [17] from a much simpler version of our model with a deterministic hydrolysis kinetics and without dimer attachment and detachment.

According to (14), GTP-tubulin dimers with larger bending angles tend to hydrolyze preferentially. If a straight GTP-dimer is bent inward ($\Delta\theta < 0°$), its hydrolysis rate is reduced according to (14); if it is bent outwards ($\Delta\theta > 0°$) the rate is increased. From the hydrolysis rates shown in **Figure 11G**, it is possible to calculate the average bending angles using (12) and (14),

$$\langle \Delta\tilde{\theta}(p,d) \rangle = \frac{1}{11°}\left[\frac{1 + \delta_{d,d(p)}}{\kappa}\ln\left(\frac{k_{\text{hydr}}(p,d)}{k_{\text{hydr}}^0}\right) + (5.5°)^2\right].$$

$$(19)$$

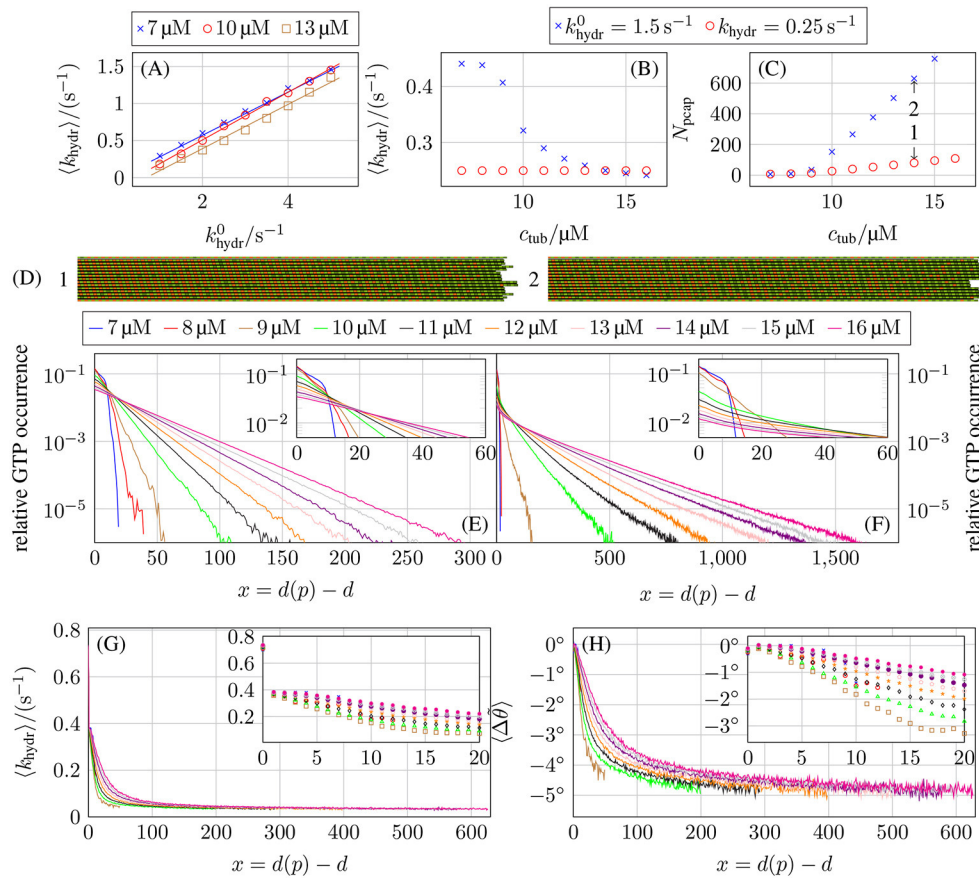**FIGURE 11 | (A)** Average actual hydrolysis rate $\langle k_{hydr}\rangle$ as a function of the constant base hydrolysis rate $k_{hydr}^0$. Comparison of **(B)** the average actual hydrolysis rate $\langle k_{hydr}\rangle$ and **(C)** the porous cap length $N_{pcap}$ as a function of the free tubulin dimer concentration $c_{tub}$ for hydrolysis coupled to mechanics with $k_{hydr}^0 = 1.5\,s^{-1}$ and a constant hydrolysis rate of $k_{hydr} = 0.25\,s^{-1}$. **(D)** Shows the two-dimensional representations of two MT tip configurations that are marked by arrows in **(C)** at $t_{sim} = 5$ min. The top and bottom protofilaments are periodic images of $p = 13$ and $p = 1$, respectively. Relative occurrence of GTP-tubulin dimers as a function of the dimer-based distance from the protofilament tip $d(p) - d$ for **(E)** a constant hydrolysis rate of $k_{hydr} = 0.25\,s^{-1}$ and **(F)** hydrolysis being coupled to mechanics and $k_{hydr}^0 = 1.5\,s^{-1}$. **(G)** Average hydrolysis rate as a function of distance $d(p) - d$ from the tip and **(H)** the associated average bending angle $\langle \Delta \tilde{\theta}\rangle$ for hydrolysis coupled to mechanics $k_{hydr}^0 = 1.5\,s^{-1}$. All plots are for $k_+ = 4\,\mu M^{-1}\,s^{-1}$, $\Delta G_{long}^{0*} = -9.3\,k_BT$, and $k_{lat} = 100\,k_BT/nm^2$.

The results for these bending angles as a function of the distance $x$ from the top are shown in **Figure 11H**. Surprisingly, almost all GTP-tubulin dimers are bent inwards ($\Delta\theta < 0°$) on average prior to hydrolysis apart from dimers close to the tip. We will interpret these results in the following.

An isolated GTP-dimer within the GDP-body can alleviate the bending stress of GDP-dimers by bending inward ($\Delta\theta < 0°$), which allows longitudinally neighboring GDP-dimers to bend outwards (such that $\Delta\theta > 0°$) resulting in an overall decrease of the MT energy (see **Figures S14, S15** in the Supplementary Material). Therefore, isolated GTP-dimers deep in the GDP-body hydrolyze with a reduced asymptotic rate $\langle k_{hydr}\rangle_\infty \ll k_{hydr}$.

We also find that, for several consecutive GTP-dimers in the same protofilament, GTP-dimers curl inward directly at the GDP/GTP interface resulting in a reduced hydrolysis rate (see **Figure S15**), while GTP-dimers in the center of a GTP-island are straight so that they have a higher hydrolysis rate than at the GDP/GTP interfaces. Effectively, this hydrolysis rate distribution

within a GTP-island results in a "anti-vectorial" hydrolysis mechanism with which GTP-islands are hydrolyzed from the interior in contrast to vectorial hydrolysis where hydrolysis happens at the GTP/GDP interfaces.

Also for GTP-dimers in layers closer to the MT tip, other longitudinally close-by GTP-dimers cooperate in alleviating bending stresses; then inward bending is still preferred, but the inward bending angle becomes smaller. This decrease in inward bending corresponds to an increase of the average hydrolysis rates $\langle k_{hydr}(x)\rangle$ for GTP-dimers in these layers compared to GTP-dimers buried deeper in the MT body (see **Figures 11G,H**). For terminal tubulin dimers ($x = 0$), we observe a hydrolysis rate $\langle k_{hydr}(x)\rangle$ *higher* than $k_{hydr}$ (while it is equal or lower than $k_{hydr}$ for all other layers $x > 0$). Hydrolysis in the first layer is enhanced because there are no tubulin dimers on top, such that hydrolysis has to overcome a smaller energy barrier as pointed out previously [the $d + 1$-term in (14) is missing corresponding to the $\delta_{d,d(p)}$-contribution in (19)].

As a result of the hydrolysis bias toward the tip, the spatial GTP-tubulin dimer distribution also differs. For concentrations where the MTs are growing only on time scales of several minutes ($c_{tub} \geq 11 \, \mu M$) for the chosen parameters, a constant hydrolysis rate leads to the expected exponential distribution of GTP-dimers shown in **Figure 11E** as observed in *in vivo* experiments [71]. Using an effective one-dimensional (or single protofilament) model similar to Padinhateeri et al. [63] to calculate the probability of tubulin dimers being GTP-tubulin dimers as a function of the polymerization rate $k_{on}$, effective depolymerization rate $\tilde{k}_{off}$, and hydrolysis rate $k_{hydr}$ matches the simulation results for concentrations at which the MTs can be considered in a steady state of growth (see section 4 in the **Supplementary Material**). We use an effective depolymerization rate $\tilde{k}_{off}$ instead of $k_{off}$, because we map onto the depolymerization process of a one-dimensional model so that $\tilde{k}_{off}$ includes all effects from lateral bond formation and rupture and the actual depolymerization process in the full model.
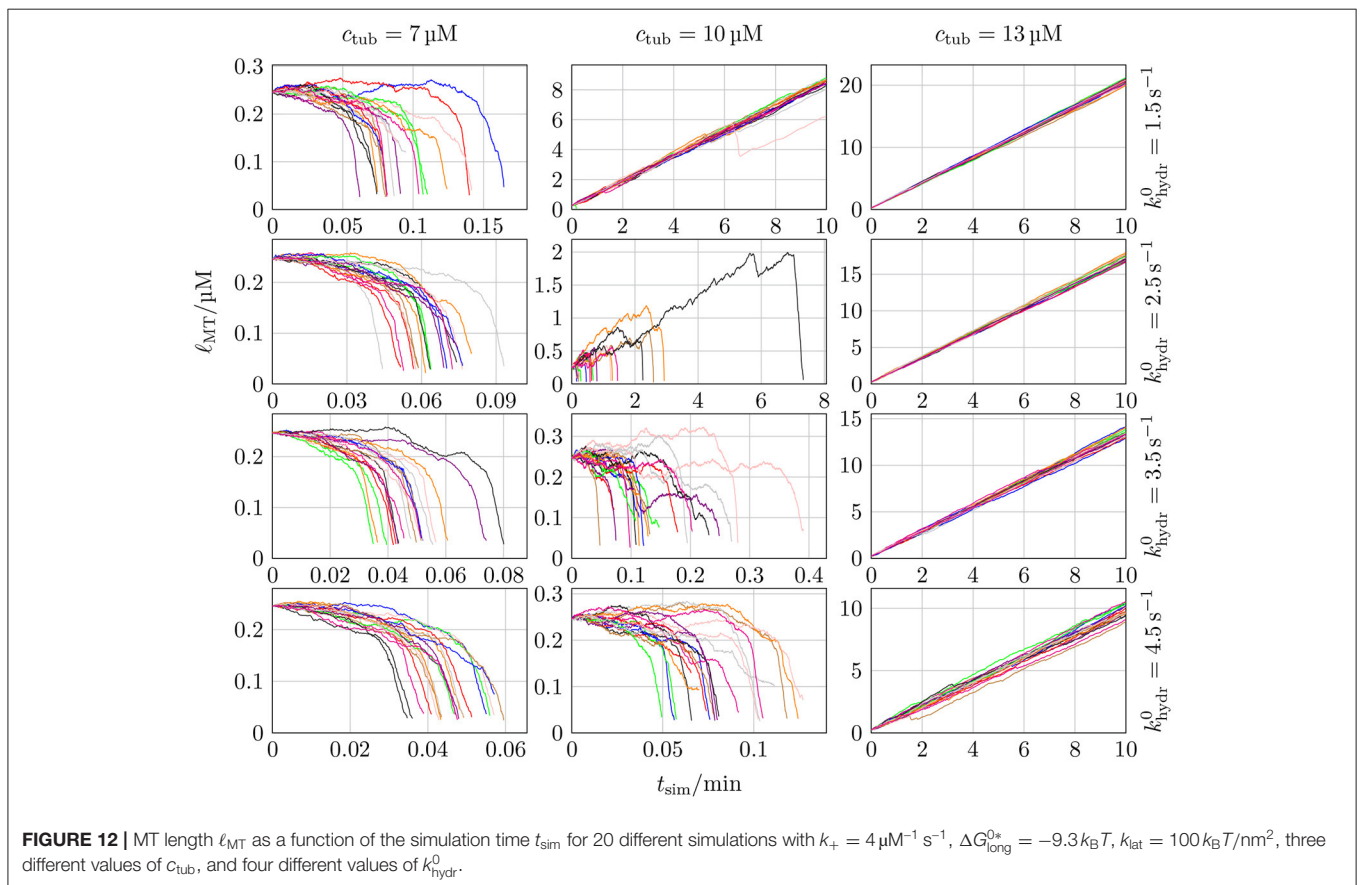
If hydrolysis is coupled to mechanics, the spatial distribution is only exponential in its tail, has larger values at the MT tip, and GTP-tubulin dimers can be found much deeper in the GDP-body (see **Figure 11F**). These results reflect that the average hydrolysis rate $\langle k_{hydr}(x) \rangle$ is decreasing toward the GDP-body and reaches a small limiting value $\langle k_{hydr} \rangle_\infty \ll k_{hydr}$ for distances $x = d(p) - d > 500$ away from the tip, which governs the exponential tail

(see **Figure 11G**). This can be rationalized by considering the probability $p_{GTP}(x)$ to find a GTP-dimer at distance $x$ from the tip in a single protofilament and continuum approximation. The balance between attachment/detachment and hydrolysis leads to

$$0 = -(k_{on} - \tilde{k}_{off}) \frac{dp_{GTP}}{dx} - \langle k_{hydr}(x) \rangle \, p_{GTP}(x) \quad (20)$$

in the stationary state, which results in a sharp initial decrease of $p_{GTP}(x)$ because $\langle k_{hydr}(0) \rangle$ is large at the tip but a much slower asymptotic exponential decrease when $\langle k_{hydr}(x) \rangle \approx \langle k_{hydr} \rangle_\infty \ll k_{hydr}$, which explains the main features in **Figure 11F**. In section 4 in the **Supplementary Material**, we show that (20) describes simulations with a constant hydrolysis and with hydrolysis coupled to mechanics equally well. With $p_{GTP}(x)$, we can define an "average cap length" as $\bar{\ell}_{cap} = \int_0^\infty dx \, p_{GTP}(x) x$. This average cap length $\bar{\ell}_{cap}$ is longer if hydrolysis is coupled to mechanics compared to a constant hydrolysis rate because $p_{GTP}(x)$ is much greater for larger $x$ (see **Figures 11E,F**). As $\bar{\ell}_{cap} < N_{pcap}$, this increase in average cap length also explains the increased porous cap length if hydrolysis is coupled to mechanics.

The relative increase of hydrolyzed GDP-dimers at the tip could make MTs more prone for catastrophes and give rise to an increased catastrophe rate and, eventually, a more realistic concentration dependence of catastrophe rates. **Figure 12**,



**FIGURE 12 |** MT length $\ell_{MT}$ as a function of the simulation time $t_{sim}$ for 20 different simulations with $k_+ = 4 \, \mu M^{-1} \, s^{-1}$, $\Delta G^{0*}_{long} = -9.3 \, k_B T$, $k_{lat} = 100 \, k_B T / nm^2$, three different values of $c_{tub}$, and four different values of $k^0_{hydr}$.
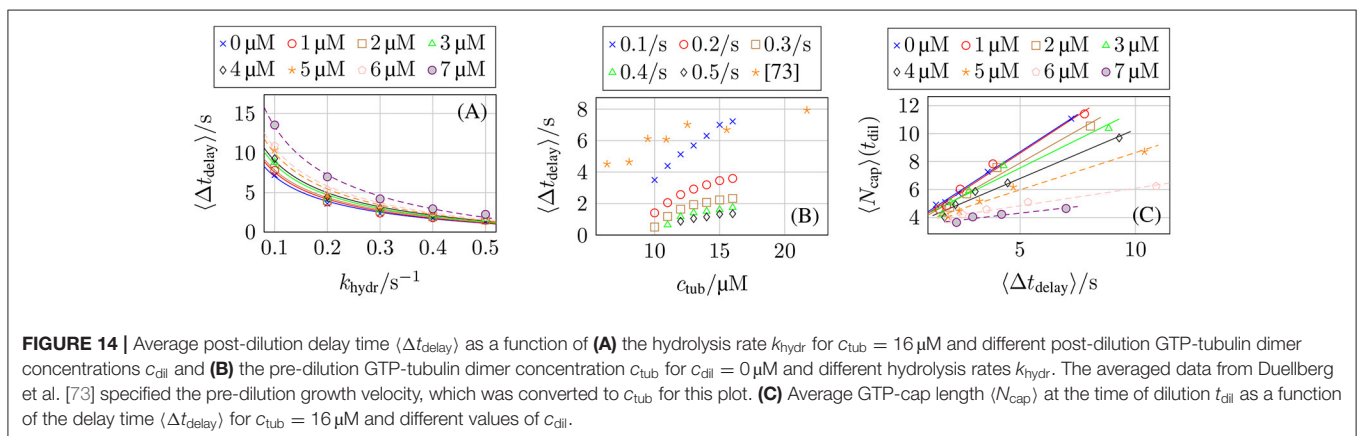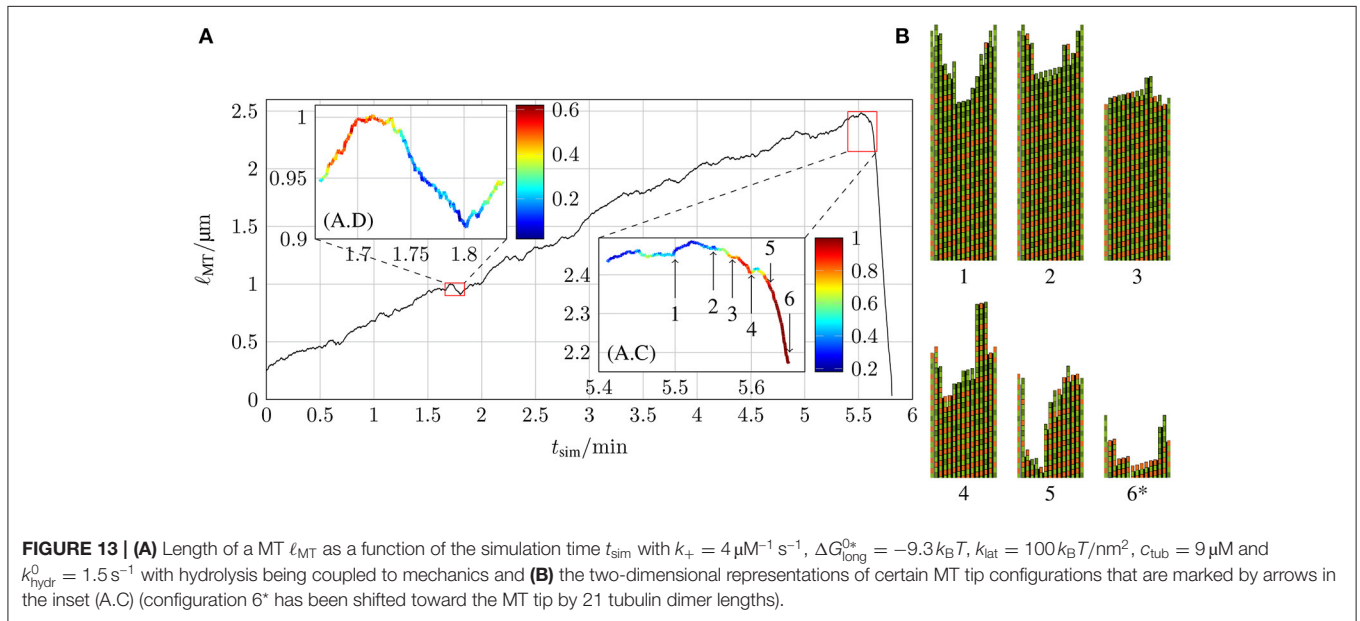
however, shows that this is not the case. Instead, the same steep dependence on the (base) hydrolysis rate as in **Figure 7** persists.

In comparison to the MT growth trajectories with a constant hydrolysis rate shown in **Figures 10**, **13** shows an example of a MT simulation in which the hydrolysis rate is coupled to mechanics. To calculate the probabilities shown in the insets, the same criteria as for **Figure 10A** were used. At first sight, these trajectories look similar to the corresponding trajectories for a constant hydrolysis rate (**Figure 10A**). There is, however, a significantly increased roughness of the trajectory during the growth phase, which could be interpreted as increased occurrence of "dips" or "stutter" events. A high probability of stutter events has also been observed in reference [35], which supports the existence of a mechanochemical coupling in hydrolysis. The catastrophe-triggering configuration of a "nucleus" of several neighboring protofilaments shrinking by more than 6 dimers is also similar as snapshots 4 and 5 in **Figure 13B** show.

## 3.8. Dilution Experiments

In dilution experiments, the free tubulin dimer concentration $c_{tub}$ is reduced to $c_{dil} \ll c_{tub}$ at a certain point in time [5, 72, 73]. If the diluted concentration is sufficiently small or zero, the GTP-cap stops growing by polymerization (and depolymerizes) but continues to hydrolyze; after a characteristic delay time $\Delta t_{delay}$, the GTP-cap has vanished, a catastrophe is initiated, and the MT shrinks. Thus, dilution experiments and their comparison to corresponding dilution simulations can give information on the hydrolysis rate. Simulation results for the delay time are shown in **Figure 14**. In the **Supplementary Material**, we explain the algorithm that we used to determine the delay time $\Delta t_{delay}$ from MT simulation trajectories in detail.

We expect the delay time to be proportional to the GTP-cap length, $\Delta t_{delay} \propto \langle N_{cap} \rangle$, as corroborated by **Figure 14C** and $\langle N_{cap} \rangle \propto \sqrt{c_{tub}/k_{hydr}}$ according to section 3.5 (see **Figures 9C,D**) [70]. This results in $\Delta t_{delay} \propto \sqrt{c_{tub}/k_{hydr}}$, which is in qualitative



**FIGURE 13 | (A)** Length of a MT $\ell_{MT}$ as a function of the simulation time $t_{sim}$ with $k_+ = 4\,\mu M^{-1}\,s^{-1}$, $\Delta G_{long}^{0*} = -9.3\,k_B T$, $k_{lat} = 100\,k_B T/nm^2$, $c_{tub} = 9\,\mu M$ and $k_{hydr}^0 = 1.5\,s^{-1}$ with hydrolysis being coupled to mechanics and **(B)** the two-dimensional representations of certain MT tip configurations that are marked by arrows in the inset (A.C) (configuration 6* has been shifted toward the MT tip by 21 tubulin dimer lengths).



**FIGURE 14 |** Average post-dilution delay time $\langle \Delta t_{delay} \rangle$ as a function of **(A)** the hydrolysis rate $k_{hydr}$ for $c_{tub} = 16\,\mu M$ and different post-dilution GTP-tubulin dimer concentrations $c_{dil}$ and **(B)** the pre-dilution GTP-tubulin dimer concentration $c_{tub}$ for $c_{dil} = 0\,\mu M$ and different hydrolysis rates $k_{hydr}$. The averaged data from Duellberg et al. [73] specified the pre-dilution growth velocity, which was converted to $c_{tub}$ for this plot. **(C)** Average GTP-cap length $\langle N_{cap} \rangle$ at the time of dilution $t_{dil}$ as a function of the delay time $\langle \Delta t_{delay} \rangle$ for $c_{tub} = 16\,\mu M$ and different values of $c_{dil}$.

agreement with our simulation data in **Figures 14A,B**. The comparison with the experimental dilution data from reference [73] in **Figure 14B** shows that delay times for a hydrolysis rate $k_{\text{hydr}} = 0.1\,s^{-1}$ come close to the experimental data but appear to depend too steeply on $c_{\text{tub}}$.

# 4. DISCUSSION

We introduced, parameterized, and analyzed a chemomechanical model for MT dynamics in which, in addition to polymerization (attachment of dimers), depolymerization (detachment of dimers), and hydrolysis of dimers, the rupture of lateral bonds between monomers in neighboring protofilaments is explicitly modeled and coupled to the mechanics of the MT. The basis for this coupling is the allosteric model according to which a hydrolyzed dimer acquires a more bent configuration, which builds up mechanical stress in the MT tubular structure via lateral bonds between dimers.

As many model parameters as possible have been determined from the experimentally measured MT growth and shrinkage velocities measured by Walker et al. [47]. To determine the values of the model parameters, we use a "divide and conquer" approach [15, 30]. We used simulations of growing GTP-only MTs to parameterize longitudinal and lateral bond energies $\Delta G_{\text{long}}^{0*}$ and $\Delta G_{\text{lat}}^{0}$ and the attempt rate $k_{\text{att}}$ for lateral bond formation. By requiring a linear concentration dependence of growth velocity, we can fix all three parameter values for a given value of $k_+$. We used simulations of shrinking GDP-only MTs to parameterize the bending constant $\kappa$ and the spring constant $k_{\text{lat}}$ of the lateral bonds. Here, we can only fix one of the two parameters. Moreover, the hydrolysis rate $k_{\text{hydr}}$ is still a free parameter, for which we use values in the range $0.1$–$0.5\,s^{-1}$ known from experiments [61].

The general philosophy of a divide-and-conquer approach is the successive fixation of simulation parameters by using first GTP-only growth, then GDP-only shrinkage and, eventually, catastrophe frequencies or dilution to fix the hydrolysis rate. This successive fixation is, however, problematic, as the corresponding experimental data is influenced by all simulation parameters in general. The problem becomes apparent when considering the hydrolysis rate: changes in the hydrolysis rate also affect the growth rate over a wide concentration range because hydrolyzed dimers have an effectively higher detachment rate, see **Figure 9B**. Strictly speaking, all simulation parameters in **Table 2** must be determined at once by fitting several experimental results simultaneously instead of the successive fixation in the divide-and-conquer approach or to apply the divide-and-conquer approach iteratively several times until a self-consistent parameter set is found. A simultaneous fixation of all parameters has been performed, for example, in reference [31] on a chemical model without bond rupture and, thus, with only four parameters (on-rate, bond energies, and hydrolysis rate). Future work on our model should include at least a re-adjustment of the parameters once a hydrolysis rate is selected such that the growth velocity of Walker et al. [47] is reproduced in the presence of hydrolysis. If

mechanical feedback onto hydrolysis is included, the model has to be re-parameterized again, in principle.

Our simulation model handles all chemical events, i.e., dimer attachment and detachment, bond rupture and formation, and hydrolysis using a Gillespie algorithm. After each chemical event, we relax the resulting MT structure mechanically by energy minimization based on the assumption that the microscopic mechanical dynamics is much faster than the chemical steps. Therefore, mechanical energy minimization is the computationally most demanding step in the simulation. This is a common problem in all dimer-based chemomechanical MT models [15, 16, 18]. We address this problem by restricting the mechanical energy minimization to bounded number MT degrees of freedom near the plus end. We showed that restricting energy minimization to a depth of $d_{\text{cutoff}} = 10$ additional layers into the MT (in minus end direction) from the point of the last chemical event is an accurate and efficient choice. Computational efficiency of this procedure is better than performing a dedicated microscopic Brownian dynamics simulation [18] and better than random local energy minimization [15, 16] (for the same accuracy in energy minimization). The restricted energy minimization strategy also ensures that the number of minimization parameters does not scale with the MT length but remains bounded, which assures that we can simulate arbitrarily long growing MTs at a fixed minimal computational speed using our approach.

Simulations do not require more than a few hours for 1 min of MT dynamics (for a constant hydrolysis rate) using just a single CPU core. Therefore, we can reach time scales of several minutes of MT dynamics which is the time scale for repeated catastrophe events for concentrations above the individual critical concentration, where the dynamic instability can occur. We performed a first systematic analysis of catastrophe and rescue rates in **Figure 8**, which indicates that the decrease of the catastrophe rate with tubulin concentration is too steep compared to experimental data [47, 66]. It is also much steeper than simulation results of reference [18] but these results for the catastrophe rate relied on linear extrapolation from unrealistically high hydrolysis rates ($3$–$11\,s^{-1}$) down to realistic values ($0.1$–$0.5\,s^{-1}$). In the future, our computational model can also be used to measure the dependence of catastrophe rates on MT lifetime [67].

Within our model, we could also study single catastrophe and rescue events in detail (see **Figure 10**). The growth paths appear very similar to experimentally observed catastrophe and rescue events. Catastrophes typically feature an initial "transitional" phase of slow shrinking by $50$–$100\,$nm as also observed in reference [35]. Moreover, we observe "dips" in the growth paths resembling the "stutter" events from reference [35].

The most interesting results of chemomechanical models are possible statements about the typical catastrophe-triggering configurations. In this respect, our simulations indicate that a catastrophe could be triggered by a "nucleus" of three neighboring protofilaments shrinking by more than 6 dimers, such that its GTP-cap is removed and its ends reach into the GDP-body of the MT. To rescue a shrinking MT the GTP-cap has to be re-established on almost all 13 protofilaments such that

nuclei of three neighboring uncapped GDP-protofilaments are avoided. This shows that mechanical correlations in the dynamics of protofilaments are important in triggering catastrophe events. This is an aspect which is absent in the calculation of catastrophe frequencies based on simplified purely chemical models, such as in reference [68], where protofilaments are regarded as effectively independent and uncorrelated.

Our model can achieve qualitative agreement with experimental data on dilution experiments (see **Figure 14C**) from reference [73] for relatively low hydrolysis rates of $k_{\text{hydr}} = 0.1 \, s^{-1}$, which is an indication that the catastrophe mechanism is correctly captured by our chemomechanical model. This also constrains the hydrolysis rate, which is still a free parameter in our model, to lower values around $k_{\text{hydr}} = 0.1 \, s^{-1}$.

Finally, we explored the consequences of a mechanochemical coupling in the hydrolysis of tubulin dimers. Because hydrolysis gives rise to bending of the GTP-dimers, we argue that mechanical forces on a dimer that increase its bending angle should also lead to higher hydrolysis rates, see (12) and (14). In the presence of mechanical feedback, hydrolysis gets a bias toward the MT plus end which, in turn, also causes an increase in porous cap length. At the same average hydrolysis rate, hydrolysis in the immediate tip of the GTP-cap is more likely while it is less likely in the remaining part of the cap such that GTP-tubulin dimers can be found much deeper in the GDP-body (see **Figure 11**). Individual catastrophe and rescue events (see **Figure 13**) look qualitatively similar in the presence of mechanical feedback but the probability of "dips" or "stutter" events is increased in agreement with reference [35]. The coupling of hydrolysis to mechanics does not increase catastrophe rates significantly such that the steep decrease of the catastrophe rate with tubulin concentration persists.

The main problem of our model appears to be the steep decrease of catastrophe rate with tubulin concentration, which could hint to a failure of basic assumptions. One possibility is that a direct effect of the hydrolysis state of the dimer onto the off-rate (as also suggested by atomistic simulations [74]) is relevant and not included in the model. Another possibility is a failure of allosteric models in general. The steep decline of catastrophe rates with the tubulin concentration gives a hint that MTs are structurally too stable for GTP-rich caps. This might provide evidence for a shortcoming of the underlying allosteric model, which inserts GTP-dimers in a straight configuration that is more prone to form stable lateral bonds than a curved configuration. An alternative are so-called lattice models [20, 21], according to which dimers are always bent but hydrolysis affects lateral and longitudinal dimer interaction energies. A systematic comparison of allosteric and lattice models toward the resulting concentration dependence of catastrophe rates within the framework provided here could help decide which class of models is more appropriate.

So far, almost all chemomechanical modeling approaches were based on the allosteric model [14–19] but recent experimental advancements in the analysis of the structure of MT tips [26] demonstrated that both growing and shrinking MTs have bent protofilament ends supporting similar earlier results [75–78]. Additionally, calculations using MT structures with different

nucleotide content in the beta-tubulin [23] and all-atom MD simulations of GTP- and GDP-only MTs [24, 25] revealed that hydrolysis weakens lateral bonds and strengthens longitudinal bonds. Both aspects support the lattice model for the influence of hydrolysis on MT mechanics. There is, however, also evidence from MD simulations for intermediate models, where hydrolysis affects interactions and also leads to a much lower GDP-tubulin flexibility [27]. Independent of these findings, our study based on the allosteric model is valuable for the following reasons: (i) In both the allosteric and the lattice model, catastrophes are cascades of lateral bond rupture and in both models, the bent shape of GDP-dimers is the dominating cause of mechanical strain in the MT structure. In the allosteric model, bending and mechanical strain is directly generated by the hydrolysis of GTP-dimers, whereas in the lattice model, the tubulin dimers are always bent but hydrolysis weakens lateral bonds. In both models, the result is an increased lateral bond rupture rate of mechanically strained bonds after hydrolysis. Therefore, an explicit modeling approach for lateral bond rupture as a stochastic process under force generated by the bending of GDP-dimers will also be important in all future chemomechanical models based on the lattice model. So far explicit stochastic models of lateral bond rupture have only been included into two-dimensional models lacking explicit mechanics [32–34] or with heavy computational cost by explicitly simulating the Brownian dynamics of dimers and bonds [18]. (ii) The importance of lateral bond rupture becomes particularly clear for shrinking MTs or MTs entering a catastrophe. In these phases of the dynamic instability, GDP-tubulin dimers are significantly more relevant than GTP-tubulin dimers. As GDP-dimers are bent in both models and this bending gives rise to lateral bond stretching, we believe that both types of models will display a very similar behavior in these phases. The only difference in this scenario is that in the lattice model, the lateral bond energy $\Delta G_{\text{lat}}^0$ in the rupture rate (10) will depend on the nucleotide type of the bonded tubulin monomers, which also makes $k_{\text{rup}}$ an explicit function of the nucleotide state. Because the nucleotide state is predominantly GDP during shrinkage, the results for properly parameterized models will be very similar. (iii) We also introduced a computationally efficient scheme to relax the mechanical energy between chemical events, which can also be employed in future chemomechanical lattice models. Within the allosteric model, we achieve a better mechanical energy relaxation than previous models [15] with significantly less computational steps than a full Brownian dynamics simulation requires [18]. (iv) The idea of a feedback of mechanical forces onto the hydrolysis rate can also be applied in future chemomechanical lattice models: if hydrolysis leads to a weakening of lateral bonds, one could expect mechanical strains that favor weakening of lateral bonds also to favor hydrolysis.

In the future, our model could be extended to also include regulating TIP+ proteins [79] for which different mechanisms of how they influence MTs could be implemented. Comparing the results of such simulations with experimental data could help to develop a mechanistic picture of the action of these proteins. Another future extension is MT polymerization under force [80, 81]. So far, polymerization under force has been investigated using chemical models [56, 82–85]; the influence

of an external force on the microscopic level, in particular the detailed dynamics of catastrophe events and the catastrophe-triggering configurations is unknown.

## DATA AVAILABILITY STATEMENT

The raw data supporting the conclusions of this article will be made available by the authors, without undue reservation.

## AUTHOR CONTRIBUTIONS

MS performed the simulations and theoretical analysis, evaluated the data, wrote, and revised the manuscript. JK conceived the research, wrote, and revised the manuscript. Both authors contributed to the article and approved the submitted version.

## FUNDING

## SUPPLEMENTARY MATERIAL

The Supplementary Material for this article can be found online at: https://www.frontiersin.org/articles/10.3389/fphy.2021.673875/full#supplementary-material

## REFERENCES

1. McIntosh JR, Grishchuk EL, West RR. Chromosome-microtubule interactions during mitosis. *Annu Rev Cell Dev Biol.* (2002) 18:193–219. doi: 10.1146/annurev.cellbio.18.032002.132412
2. Siegrist SE, Doe CQ. Microtubule-induced cortical cell polarity. *Genes Dev.* (2007) 21:483–96. doi: 10.1101/gad.1511207
3. Mitchison T, Kirschner M. Dynamic instability of microtubule growth. *Nature.* (1984) 312:237–42. doi: 10.1038/312237a0
4. Carlier MF, Hill TL, Chen Yd. Interference of GTP hydrolysis in the mechanism of microtubule assembly: an experimental study. *Proc Natl Acad Sci USA.* (1984) 81:771–5. doi: 10.1073/pnas.81.3.771
5. Walker RA, Pryer NK, Salmon ED. Dilution of individual microtubules observed in real time *in vitro*: evidence that cap size is small and independent of elongation rate. *J Cell Biol.* (1991) 114:73–81. doi: 10.1083/jcb.114.1.73
6. Howard J, Hyman AA. Growth, fluctuation and switching at microtubule plus ends. *Nat Rev Mol Cell Biol.* (2009) 10:569–74. doi: 10.1038/nrm2713
7. van Haren J, Wittmann T. Microtubule plus end dynamics-do we know how microtubules grow? *Bioessays.* (2019) 41:1800194. doi: 10.1002/bies.201800194
8. Mandelkow EM, Mandelkow E, Milligan RA. Microtubule dynamics and microtubule caps: a time-resolved cryo-electron microscopy study. *J Cell Biol.* (1991) 114:977–91. doi: 10.1083/jcb.114.5.977
9. McIntosh JR, Volkov V, Ataullakhanov FI, Grishchuk EL. Tubulin depolymerization may be an ancient biological motor. *J Cell Sci.* (2010) 123:3425–34. doi: 10.1242/jcs.067611
10. Müller-Reichert T, Chrétien D, Severin F, Hyman AA. Structural changes at microtubule ends accompanying GTP hydrolysis: Information from a slowly hydrolyzable analogue of GTP, guanylyl $(\alpha,\beta)$ methylenediphosphonate. *Proc Natl Acad Sci USA.* (1998) 95:3661–6. doi: 10.1073/pnas.95.7.3661
11. Downing KH, Eva N. Tubulin and microtubule structure. *Curr Opin Cell Biol.* (1998) 10:16–22. doi: 10.1016/S0955-0674(98)80082-3
12. Nogales E, Wang HW. Structural mechanisms underlying nucleotide-dependent self-assembly of tubulin and its relatives. *Curr Opin Struct Biol.* (2006) 16:221–9. doi: 10.1016/j.sbi.2006.03.005
13. Nogales E, Whittaker M, Milligan RA, Downing KH. High-resolution model of the microtubule. *Cell.* (1999) 96:79–88. doi: 10.1016/S0092-8674(00)80961-7
14. Molodtsov MI, Ermakova EA, Shnol EE, Grishchuk EL, McIntosh JR, Ataullakhanov FI. A molecular-mechanical model of the microtubule. *Biophys J.* (2005) 88:3167–79. doi: 10.1529/biophysj.104.051789
15. VanBuren V, Cassimeris L, Odde DJ. Mechanochemical model of microtubule structure and self-assembly kinetics. *Biophys J.* (2005) 89:2911–26. doi: 10.1529/biophysj.105.060913
16. Coombes C, Yamamoto A, Kenzie M, Odde D, Gardner M. Evolving tip structures can explain age-dependent microtubule catastrophe. *Curr Biol.* (2013) 23:1342–8. doi: 10.1016/j.cub.2013.05.059
17. Müller N, Kierfeld J. Effects of microtubule mechanics on hydrolysis and catastrophes. *Phys Biol.* (2014) 11:046001. doi: 10.1088/1478-3975/11/4/046001
18. Zakharov P, Gudimchuk N, Voevodin V, Tikhonravov A, Ataullakhanov F, Grishchuk E. Molecular and mechanical causes of microtubule catastrophe and aging. *Biophys J.* (2015) 109:2574–91. doi: 10.1016/j.bpj.2015.10.048
19. Jain I, Inamdar MM, Padinhateeri R. Statistical mechanics provides novel insights into microtubule stability and mechanism of shrinkage. *PLoS Comput Biol.* (2015) 11:e1004099. doi: 10.1371/journal.pcbi.1004099
20. Buey RM, Díaz JF, Andreu JM. The nucleotide switch of tubulin and microtubule assembly: a polymerization-driven structural change. *Biochemistry.* (2006) 45:5933–8. doi: 10.1021/bi060334m
21. Rice LM, Montabana EA, Agard DA. The lattice as allosteric effector: structural studies of $\alpha\beta$- and $\gamma$-tubulin clarify the role of GTP in microtubule assembly. *Proc Natl Acad Sci USA.* (2008) 105:5378–83. doi: 10.1073/pnas.0801155105
22. Alushin GM, Lander GC, Kellogg EH, Zhang R, Baker D, Nogales E. High-resolution microtubule structures reveal the structural transitions in $\alpha\beta$-tubulin upon GTP hydrolysis. *Cell.* (2014) 157:1117–29. doi: 10.1016/j.cell.2014.03.053
23. Manka SW, Moores CA. The role of tubulin–tubulin lattice contacts in the mechanism of microtubule dynamic instability. *Nat Struct Mol Biol.* (2018) 25:607–15. doi: 10.1038/s41594-018-0087-8
24. Ayoub AT, Klobukowski M, Tuszynski JA. Detailed per-residue energetic analysis explains the driving force for microtubule disassembly. *PLoS Comput Biol.* (2015) 11:e1004313. doi: 10.1371/journal.pcbi.1004313
25. Fedorov VA, Orekhov PS, Kholina EG, Zhmurov AA, Ataullakhanov FI, Kovalenko IB, et al. Mechanical properties of tubulin intra- and inter-dimer interfaces and their implications for microtubule dynamic instability. *PLoS Comput Biol.* (2019) 15:e1007327. doi: 10.1371/journal.pcbi.1007327
26. McIntosh JR, O'Toole E, Morgan G, Austin J, Ulyanov E, Ataullakhanov F, et al. Microtubules grow by the addition of bent guanosine triphosphate tubulin to the tips of curved protofilaments. *J Cell Biol.* (2018) 217:2691–708. doi: 10.1083/jcb.201802138
27. Igaev M, Grubmüller H. Microtubule assembly governed by tubulin allosteric gain in flexibility and lattice induced fit. *Elife.* (2018) 7:e34353. doi: 10.7554/eLife.34353.041
28. Zakharov PN, Arzhanik VK, Ulyanov EV, Gudimchuk NB, Ataullakhanov FI. Microtubules: dynamically unstable stochastic phase-switching polymers. *Phys Uspekhi.* (2016) 59:773–86. doi: 10.3367/UFNe.2016.04.037779
29. Dogterom M, Leibler S. Physical aspects of the growth and regulation of microtubule structures. *Phys Rev Lett.* (1993) 70:1347–50. doi: 10.1103/PhysRevLett.70.1347

30. VanBuren V, Odde DJ, Cassimeris L. Estimates of lateral and longitudinal bond energies within the microtubule lattice. *Proc Natl Acad Sci USA*. (2002) 99:6035–40. doi: 10.1073/pnas.092504999

31. Piette BMAG, Liu J, Peeters K, Smertenko A, Hawkins T, Deeks M, et al. A thermodynamic model of microtubule assembly and disassembly. *PLoS ONE*. (2009) 4:e6378. doi: 10.1371/journal.pone.0006378

32. Margolin G, Goodson HV, Alber MS. Mean-field study of the role of lateral cracks in microtubule dynamics. *Phys Rev E*. (2011) 83:041905. doi: 10.1103/PhysRevE.83.041905

33. Margolin G, Gregoretti IV, Cickovski TM, Li C, Shi W, Alber MS, et al. The mechanisms of microtubule catastrophe and rescue: implications from analysis of a dimer-scale computational model. *Mol Biol Cell*. (2012) 23:642–56. doi: 10.1091/mbc.e11-08-0688

34. Li C, Li J, Goodson HV, Alber MS. Microtubule dynamic instability: the role of cracks between protofilaments. *Soft Matter*. (2014) 10:2069–80. doi: 10.1039/C3SM52892H

35. Mahserejian SM, Scripture JP, Mauro AJ, Lawrence EJ, Jonasson EM, Murray KS, et al. Stutter: a transient dynamic instability phase that is strongly associated with catastrophe. *bioRxiv*. (2019). doi: 10.1101/2019.12.16.878603

36. Wang HW, Nogales E. Nucleotide-dependent bending flexibility of tubulin regulates microtubule assembly. *Nature*. (2005) 435:911–5. doi: 10.1038/nature03606

37. VanBuren V, Odde DJ, Cassimeris L. Errata for VanBuren et al., Estimates of lateral and longitudinal bond energies within the microtubule lattice, PNAS 2002 99:6035–6040. *Proc Natl Acad Sci USA*. (2004) 101:14989. doi: 10.1073/pnas.0406393101

38. Harris BJ, Ross JL, Hawkins TL. Microtubule seams are not mechanically weak defects. *Phys Rev E*. (2018) 97:062408. doi: 10.1103/PhysRevE.97.062408

39. Elie-Caille C, Severin F, Helenius J, Howard J, Muller DJ, Hyman AA. Straight GDP-tubulin protofilaments form in the presence of taxol. *Curr Biol*. (2007) 17:1765–70. doi: 10.1016/j.cub.2007.08.063

40. Kroy K, Frey E. Dynamic scattering from solutions of semiflexible polymers. *Phys Rev E*. (1997) 55:3092–101. doi: 10.1103/PhysRevE.55.3092

41. Ulyanov EV, Vinogradov DS, McIntosh JR, Gudimchuk NB. Brownian dynamics simulation of protofilament relaxation during rapid freezing. *PLoS ONE*. (2021) 16:e0247022. doi: 10.1371/journal.pone.0247022

42. Gardner M, Charlebois B, Jánosi I, Howard J, Hunt A, Odde D. Rapid microtubule self-assembly kinetics. *Cell*. (2011) 146:582–92. doi: 10.1016/j.cell.2011.06.053

43. Kononova O, Kholodov Y, Theisen KE, Marx KA, Dima RI, Ataullakhanov FI, et al. Tubulin bond energies and microtubule biomechanics determined from nanoindentation *in silico*. *J Am Chem Soc*. (2014) 136:17036–45. doi: 10.1021/ja506385p

44. Bell GI. Models for the specific adhesion of cells to cells. *Science*. (1978) 200:618–27. doi: 10.1126/science.347575

45. Evans E, Ritchie K. Dynamic strength of molecular adhesion bonds. *Biophys J*. (1997) 72:1541–55. doi: 10.1016/S0006-3495(97)78802-7

46. Gillespie DT. A general method for numerically simulating the stochastic time evolution of coupled chemical reactions. *J Comput Phys*. (1976) 22:403–34. doi: 10.1016/0021-9991(76)90041-3

47. Walker RA, O'Brien ET, Pryer NK, Soboeiro MF, Voter WA, Erickson HP, et al. Dynamic instability of individual microtubules analyzed by video light microscopy: rate constants and transition frequencies. *J Cell Biol*. (1988) 107:1437–48. doi: 10.1083/jcb.107.4.1437

48. O'Brien ET, Salmon ED, Walker RA, Erickson HP. Effects of magnesium on the dynamic instability of individual microtubules. *Biochemistry*. (1990) 29:6648–56. doi: 10.1021/bi00480a014

49. Drechsel DN, Hyman AA, Cobb MH, Kirschner MW. Modulation of the dynamic instability of tubulin assembly by the microtubule-associated protein tau. *Mol Biol Cell*. (1992) 3:1141–54. doi: 10.1091/mbc.3.10.1141

50. Trinczek B, Marx A, Mandelkow EM, Murphy DB, Mandelkow E. Dynamics of microtubules from erythrocyte marginal bands. *Mol Biol Cell*. (1993) 4:323–35. doi: 10.1091/mbc.4.3.323

51. Chrétien D, Fuller SD, Karsenti E. Structure of growing microtubule ends: two-dimensional sheets close into tubes at variable rates. *J Cell Biol*. (1995) 129:1311–28. doi: 10.1083/jcb.129.5.1311

52. Pedigo S, Williams RC Jr. Concentration dependence of variability in growth rates of microtubules. *Biophys J*. (2002) 83:1809–19. doi: 10.1016/S0006-3495(02)73946-5

53. Galassi M, Davies J, Theiler J, Gough B, Jungman G, Alken P, et al. *GNU Scientific Library Reference Manual*. Available online at: https://www.gnu.org/software/gsl/

54. Ayaz P, Munyoki S, Geyer EA, Piedra FA, Vu ES, Bromberg R, et al. A tethered delivery mechanism explains the catalytic action of a microtubule polymerase. *eLife*. (2014) 3:e03069. doi: 10.7554/eLife.03069.014

55. Mickolajczyk KJ, Geyer EA, Kim T, Rice LM, Hancock WO. Direct observation of individual tubulin dimers binding to growing microtubules. *Proc Natl Acad Sci USA*. (2019) 116:7314–22. doi: 10.1073/pnas.1815823116

56. Stukalin EB, Kolomeisky AB. Simple growth models of rigid multifilament biopolymers. *J Chem Phys*. (2004) 121:1097–104. doi: 10.1063/1.1759316

57. Sim H, Sept D. Properties of microtubules with isotropic and anisotropic mechanics. *Cell Mol Bioeng*. (2013) 6:361–8. doi: 10.1007/s12195-013-0302-y

58. Driver JW, Geyer EA, Bailey ME, Rice LM, Asbury CL. Direct measurement of conformational strain energy in protofilaments curling outward from disassembling microtubule tips. *eLife*. (2017) 6:e28433. doi: 10.7554/eLife.28433.023

59. Deriu MA, Enemark S, Soncini M, Montevecchi FM, Redaelli A. Tubulin: from atomistic structure to supramolecular mechanical properties. *J Mater Sci*. (2007) 42:8864–72. doi: 10.1007/s10853-007-1784-6

60. Grafmüller A, Voth G. Intrinsic bending of microtubule protofilaments. *Structure*. (2011) 19:409–17. doi: 10.1016/j.str.2010.12.020

61. Melki R, Fievez S, Carlier MF. Continuous monitoring of $P_i$ release following nucleotide hydrolysis in actin or tubulin assembly using 2-amino-6-mer-capto-7-methylpurine ribonucleoside and purine-nucleoside phosphorylase as an enzyme-linked assay. *Biochemistry*. (1996) 35:12038–45. doi: 10.1021/bi961325o

62. Aparna JS, Padinhateeri R, Das D. Signatures of a macroscopic switching transition for a dynamic microtubule. *Sci Rep*. (2017) 7:45747. doi: 10.1038/srep45747

63. Padinhateeri R, Kolomeisky A, Lacoste D. Random hydrolysis controls the dynamic instability of microtubules. *Biophys J*. (2012) 102:1274–83. doi: 10.1016/j.bpj.2011.12.059

64. Bowne-Anderson H, Zanic M, Kauer M, Howard J. Microtubule dynamic instability: a new model with coupled GTP hydrolysis and multistep catastrophe. *Bioessays*. (2013) 35:452–61. doi: 10.1002/bies.201200131

65. Piedra FA, Kim T, Garza ES, Geyer EA, Burns A, Ye X, et al. GDP-to-GTP exchange on the microtubule end can contribute to the frequency of catastrophe. *Mol Biol Cell*. (2016) 27:3515–25. doi: 10.1091/mbc.e16-03-0199

66. Janson ME, de Dood ME, Dogterom M. Dynamic instability of microtubules is regulated by force. *J Cell Biol*. (2003) 161:1029–34. doi: 10.1083/jcb.200301147

67. Gardner M, Zanic M, Gell C, Bormuth V, Howard J. Depolymerizing kinesins Kip3 and MCAK shape cellular microtubule architecture by differential control of catastrophe. *Cell*. (2011) 147:1092–103. doi: 10.1016/j.cell.2011.10.037

68. Flyvbjerg H, Holy TE, Leibler S. Microtubule dynamics: caps, catastrophes, and coupled hydrolysis. *Phys Rev E*. (1996) 54:5538–60. doi: 10.1103/PhysRevE.54.5538

69. Zelinski B, Kierfeld J. Cooperative dynamics of microtubule ensembles: polymerization forces and rescue-induced oscillations. *Phys Rev E*. (2013) 87:012703. doi: 10.1103/PhysRevE.87.012703

70. Li X, Lipowsky R, Kierfeld J. Coupling of actin hydrolysis and polymerization: reduced description with two nucleotide states. *Europhys Lett*. (2011) 89:38010. doi: 10.1209/0295-5075/89/38010

71. Seetapun D, Castle B, McIntyre A, Tran P, Odde D. Estimating the microtubule GTP cap size *in vivo*. *Curr Biol*. (2012) 22:1681–7. doi: 10.1016/j.cub.2012.06.068

72. Voter WA, O'Brien ET, Erickson HP. Dilution-induced disassembly of microtubules: relation to dynamic instability and the GTP cap. *Cell Motil Cytoskeleton*. (1991) 18:55–62. doi: 10.1002/cm.970180106

73. Duellberg C, Cade NI, Holmes D, Surrey T. The size of the EB cap determines instantaneous microtubule stability. *eLife*. (2016) 5:e13470. doi: 10.7554/eLife.13470.023

74. Grafmüller A, Noya EG, Voth GA. Nucleotide-dependent lateral and longitudinal interactions in microtubules. *J Mol Biol*. (2013) 425:2232–46. doi: 10.1016/j.jmb.2013.03.029

75. Höög JL, Huisman SM, Sebö-Lemke Z, Sandblad L, McIntosh JR, Antony C, et al. Electron tomography reveals a flared morphology on

growing microtubule ends. *J Cell Sci*. (2011) 124:693–8. doi: 10.1242/jcs.0 72967

76. Kukulski W, Schorb M, Welsch S, Picco A, Kaksonen M, Briggs JAG. Correlated fluorescence and 3D electron microscopy with high sensitivity and spatial precision. *J Cell Biol*. (2011) 192:111–9. doi: 10.1083/jcb.2010 09037

77. Nawrotek A, Knossow M, Gigant B. The determinants that govern microtubule assembly from the atomic structure of GTP-tubulin. *J Mol Biol*. (2011) 412:35–42. doi: 10.1016/j.jmb.2011.07.029

78. Pecqueur L, Duellberg C, Dreier B, Jiang Q, Wang C, Plückthun A, et al. A designed ankyrin repeat protein selected to bind to tubulin caps the microtubule plus end. *Proc Natl Acad Sci USA*. (2012) 109:12011–16. doi: 10.1073/pnas.1204129109

79. Akhmanova A, Steinmetz MO. Tracking the ends: a dynamic protein network controls the fate of microtubule tips. *Nat Rev Mol Cell Biol*. (2008) 9:309–22. doi: 10.1038/nrm2369

80. Dogterom M, Yurke B. Measurement of the force-velocity relation for growing microtubules. *Science*. (1997) 278:856–60. doi: 10.1126/science.278.5339.856

81. Dogterom M, Kerssemakers JWJ, Romet-Lemonne G, Janson ME. Force generation by dynamic microtubules. *Curr Opin Cell Biol*. (2005) 17:67–74. doi: 10.1016/j.ceb.2004.12.011

82. van Doorn GS, Tǎnase C, Mulder BM, Dogterom M. On the stall force for growing microtubules. *Eur Biophys J*. (2000) 29:2–6. doi: 10.1007/s002490050245

83. Kolomeisky AB, Fisher ME. Force-velocity relation for growing microtubules. *Biophys J*. (2001) 80:149–54. doi: 10.1016/S0006-3495(01)76002-X

84. Ranjith P, Lacoste D, Mallick K, Joanny JF. Nonequilibrium self-assembly of a filament coupled to ATP/GTP hydrolysis. *Biophys J*. (2009) 96:2146–59. doi: 10.1016/j.bpj.2008.12.3920

85. Krawczyk J, Kierfeld J. Stall force of polymerizing microtubules and filament bundles. *Europhys Lett*. (2011) 93:28006. doi: 10.1209/0295-5075/93/28006